INVESTIGATION OF DC GENERATED PLASMAS USING TERAHERTZ TIME DOMAIN SPECTROSCOPY

A THESIS SUBMITTED TO
THE GRADUATE SCHOOL OF NATURAL AND APPLIED SCIENCES
OF
MIDDLE EAST TECHNICAL UNIVERSITY

BY
GÜLTEN KARAOĞLAN

IN PARTIAL FULFILLMENT OF THE REQUIREMENTS
FOR
THE DEGREE OF MASTER OF SCIENCE
IN
PHYSICS

MAY 2010

Approval of the Thesis:

INVESTIGATION OF DC GENERATED PLASMAS USING TERAHERTZ TIME DOMAIN SPECTROSCOPY

Submitted by **GÜLTEN KARAOĞLAN** in partial fulfillment of the requirements for the degree of **Master of Science in Physics Department, Middle East Technical University** by,

Prof. Dr. Canan Özgen _____
Dean, Graduate School of **Natural and Applied Sciences**

Prof. Dr. Sinan Bilikmen _____
Head of Department, **Physics**

Assist. Prof. Dr. Hakan Altan _____
Supervisor, **Physics Dept., METU**

Examining Committee Members:

Prof. Dr. Sinan Bilikmen _____
Physics Dept., METU

Assist. Prof. Dr. Hakan Altan _____
Physics Dept., METU

Prof. Dr. Ramazan Aydın _____
Physics Group, Atılım University

Assoc.Prof. Dr. Serhat Çakır _____
Physics Dept., METU

Dr. Halil Berberoğlu _____
Physics Dept., METU

Date: 25.05.2010

I hereby declare that all information in this document has beeen obtained and presented in accordance with acedemic rules and ethical conduct. I also declare that, as required by these rules and conduct, I have fully cited and referenced all material and results that are not original to this work.

Name, Last name : Gülten Karaoğlan

Signature :

ABSTRACT

INVESTIGATION OF DC GENERATED PLASMAS USING TERAHERTZ TIME-DOMAIN SPECTROSCOPY

Karaoğlan, Gülten
M.S. Department of Physics
Supervisor: Assist. Prof. Dr. Hakan Altan

May 2010, 84 pages

This thesis is on the topic of investigation of the characteristics of DC Glow Discharge plasmas. Emphasis is given on characterizing the plasma electron density. The methods of generating and detecting THz pulses are described. THz transmission spectroscopy and plasma emission spectroscopy is examined. Transmission spectrum is taken for Air, gaseous Nitrogen and Argon plasmas. Moreover, emission spectrum of Air, N_2 and Ar plasma analysis were done respectively. It was found that the transmission of terahertz pulses through nitrogen plasma was considerably affected compared to that of the argon plasma. Initially Drude model theory of electron conduction is employed to analyze the plasma density.

Keywords: THz-TDS, terahertz, DC Glow Discharge, Drude Model, Dielectric Function

ÖZ

DOĞRU AKIM İLE ELDE EDİLEN PLAZMALARIN ÖZELLİKLERİNİN ATIMLI TERAHERTZ SPECTROSCOPİ İLE İNCELENMESİ

Karaoğlan, Gülten
Yüksek Lisans, Fizik Bölümü
Tez Yöneticisi: Yrd. Doç. Dr. Hakan Altan

Mayıs 2010, 84 sayfa

Bu tezde dc bosalmalı plazma karakterizasyonu yapılmıştır. Plasma elektron yoğunluğunun belirlenmesine önem verilmiştir. Terahertz atımlarının üretilmesi ve ölçülmesi açıklanmıştır. Terahertz dalgalarının plasmadan geçişleri ve plasma emisyon ölçümleri alınıp bu tezde anlatılmıştır. Terahertz plasma geçiş ölçümleri hava, gas nitrojen ve argon plasmalar icin alınmıştır. Hava, N_2 ve Ar plasmalar icin emisyon ölçümleri yapılmıştır. Bu ölçümler sonunda terahertzin nitrogen ve hava plasmalarından gecislerinden etkilendiği ama argon plasma geçişinden etkilenmediği gözlemlenmiştir. Plasma electron yoğunluğunu analiz edebilmek icin Drude Modeli kullanılmıştır.

Anahtar Kelimeler: THz-TDS, terahertz, DC boşalmalı plasma, Drude Modeli, Dielectric Fonksiyonu

To my family

ACKNOWLEDGEMENTS

First off all, I would like to thank my advisor Assist. Prof. Dr. Hakan Altan for his introducing me into the topic, for his patient guidance and support. My special thanks belong to the members of the THz group at METU for the helpful and friendly atmosphere, especially my lab partners Zahide Tosun and Kamil Çınar for creating a very productive working environment. I would like to thank Demiral Akbar for his discussions on plasma. Also, I would like to express my thanks to my colleagues and the staff at Atılım University Physics Group for their understanding and patience. My special thanks goes to Bahadir Bebek for his never ending support, assistance and encouragement. I would like to thank Nazan Kara for her friendship and sharing. I also thank all other friends for their support in this journey. Many thanks are due to our cats Çıtır and ZuZu for their help on keeping me awake and for relaxing me. Last but not least, I would like to express my appreciation especially to my family, who supported and encouraged me all throughout these years, without them my university studies would not be possible.

TABLE OF CONTENTS

ABSTRACT iv

ÖZ v

ACKNOWLEDGEMENTS vii

TABLE OF CONTENTS viii

LIST OF TABLES x

LIST OF FIGURES xi

CHAPTERS

1. INTRODUCTION 1

2. PRINCIPLES OF TERAHERTZ SPECTROSCOPY 6

2.1 Terahertz Generation: 6

2.1.1 Photoconductive Antenna: 7

2.1.2 Optical Rectification: 13

2.2 Terahertz Detection: 16

2.2.1 Photoconductive Detection 16

2.2.2 Electro-Optic Detection 19

2.3 Terahertz Time Domain Spectroscopy: 22

2.3.1 Photoconductive Sampling 24

2.3.2 Electro-Optic Sampling 26

2.3.3 Electro-Optic Sampling vs Photoconductive Sampling 27

3. LOW TEMPERATURE PLASMA 28
3.1 Introduction 28
3.2 DC Glow Discharge: 30
3.2.1 Excitation and Ionization: 34
3.2.2 Anode: 36
3.2.3 Cathode: 37
3.3 Electromagnetic Waves in Plasma: 38
4. DESCRIPTION OF EXPERIMENTS 45
4.1 THz TDS System: 45
4.2 Vacuum and DC Bias System: 53
4.3 Emission Spectroscopy 57
5. EXPERIMENTAL RESULTS 59
5.1 Air Plasma 63
5.2 Gas Plasma 68
5.2.1 Emission Spectrum: 69
5.2.2 Transmission Spectrum: 70
6. CONCLUSION 76
REFERENCES 79

LIST OF TABLES

TABLES;

Table 1.1 Electromagnetic Spectrum..... 2

Table 2.1 Characteristics of photoconductive materials..... 11

Table 2.2 Properties of Typical Electro-optic Sensor Crystals..... 21

Table 3.1 Values of coefficients A and B for various gases..... 31

Table 4.1 Electrical Properties of the PCA-44-06-10-800-x [62]..... 47

Table 4.2 Optical excitation parameters of PCA-44-06-10-800-x [62]..... 48

Table 4.3 Electrical Properties of the PCA-40-05-10-800-x [63]..... 50

Table 4.4 Optical excitation parameters of PCA-40-05-10-800-x [63]..... 51

Table 4.5 Applied potential and plasma potential data for changing current and pressure values for different plasma types..... 55

Table 5.1 Observed emission lines of N_2 and Ar with their corresponding species..... 70

Table 5.2 Ionization processes of N_2 and Ar plasma species along with their ionization energies..... 74

Table 5.3 Comparison of breakdown voltage and secondary ionization coefficient for N_2 and Ar..... 75

LIST OF FIGURES

FIGURES;

Figure 2.1 Illustration of a basic photoconductive switch..... 7

Figure 2.2 THz generation by photon absorption..... 8

Figure 2.3 Basic Hertzian Dipole..... 9

Figure 2.4 Types of antenna (a) bowtie antenna (b) dipole antenna (c) coplanar stripline..... 10

Figure 2.5 Antenna mounted on a hemispherical silicon lens..... 12

Figure 2.6 Illustration of beam collimation by hemispherical silicon lens..... 12

Figure 2.7 Illustration of optical rectification (the generated pulse is the envelope of the optical pulse [29])..... 13

Figure 2.8 Illustration oh THz generation with optical rectification for two different incident pulse [22]..... 14

Figure 2.9 Schematic view of a typical pc antenna detector ……..… 16

Figure 2.10 A figure illustrating the measurement of THz pulse using photoconductive sampling: The bottom frame shows the corresponding measured THz waveform, with four specific frame is marked [22]..... 18

Figure 2.11 Detection by electro-optic sampling [22] 20

Figure 2.12 Typical set up for THz-TDS 22

Figure 2.13 A typical pc sampling set up 25

Figure 2.14 A typical set for EO Sampling…….…….. 26

Figure 3.1 DC Discharge experimental Set-up 31

Figure 3.2 Paschen Curve for some gases 32

Figure 3.3 Typical distribution of glow [46]..... 33

Figure 3.4 V-I Characteristics of Glow Discharge [48] ……..... 34

Figure 3.5 Real part of refractive index for various electron densities 40

Figure 3.6 Imaginery part of refractive index for various electron densities .. 41

Figure 3.7 Real part of the conductivity 41

Figure 3.8 Imaginary part of the conductivity 42

Figure 3.9 Illustration of one layer plasma 42

Figure 3.10 Transmission between 0.01 THz and 1 THz for electron densities 10^9 to 10^{11}..... 43

Figure 3.11 Transmission between 0.01 THz and 1 THz for electron densities 10^{11} to 10^{13}..... 44

Figure 4.1 THz-TDS System for plasma diagnostics..... 46

Figure 4.2 Photo and schematic diagram of the PCA-44-06-10-800-x [62].... 48

Figure 4.3 Schematic diagram of PCA-40-05-10-800-x [63]..... 50

Figure 4.4 Photograph of the set up in the laboratory. The plasma chamber was built using the inductrial manufacturing capabilities of the industry in Ankara, Turkey. The plasma chamber consists of two 12cm diameter steel electrodes with ad adjustable gap distance which was generally kept larger than the THz beam path of 50mm (This distance was actually kept closer to 9cm to probe the positive and negative regions of the plasma effectively)..... 52

Figure 4.5 Vacuum System..... 53

Figure 4.6 Electrical connections of the set up. The typical values of measured potentials by the voltmeter and measured current by ammeter is given in Table 4.6. The resistance values are..... 56

Figure 5.1 Orientation of DC electric field and THz electric field. The figure on the left hand side gives the perpendicular polarization and the figure on the right hand side gives the parallel polarization..... 60

Figure 5.2 Dimensions of plasma chamber..... 61

Figure 5.3 The THz pulse, passing through 0.1 torr air plasma with plasma current 15 mA and vacuum when the THz electric field is perpendicular to the DC electric field…….…..... 62

Figure 5.4 Photographic image of atmospheric plasma……... 64

Figure 5.5 THz transmission through air DC glow discharge plasma for different pressures and plasma currents from anode region and parallel polarization……. 65

Figure 5.6 THz transmission through air DC glow discharge plasma for different pressures and plasma currents from cathode region and parallel polarization……. 65

Figure 5.7 THz transmission through air DC glow discharge plasma for different pressures and plasma currents from anode region and perpendicular polarization……...… 66

Figure 5.8 THz transmission through air DC glow discharge plasma for different pressures and plasma currents from cathode region and perpendicular polarization……... 67

Figure 5.9 200 nm- 1100 nm Emission Spectrum of Air, N_2 and Ar Gas Plasmas respectively……...…… 69

Figure 5.10 THz transmission through N_2 DC glow discharge plasma for different pressures and plasma currents from anode region and perpendicular polarization……... 71

Figure 5.11 THz transmission through N_2 DC glow discharge plasma for different pressures and plasma currents from cathode region and perpendicular polarization……..……. 72

Figure 5.12 THz transmission through Ar DC glow discharge plasma for different pressures and plasma currents from anode region and perpendicular polarization……... 72

Figure 5.13 THz transmission through Ar DC glow discharge plasma for different pressures and plasma currents from cathode region and perpendicular polarization…….. 73

CHAPTER 1

INTRODUCTION

Although Terahertz (THz) signals have been observed previously, the appearance of Terahertz technology has occurred very recently due to the lack of generation and detection of electromagnetic waves at these wavelengths. The development in ultrafast lasers and optics has allowed the terahertz field to become known as a new area of research. Differing from far-IR studies, THz techniques allow us to carry out time resolved studies with subpicosecond temporal resolution based on the fact that THz pulses are created and detected using ultrashort pulsed visible lasers [1]. As it generally known to be an unexplored area of physics there are a lot of things to do for researchers. THz waves lies in the frequency range between 0.1 THz and 10 THz. 1 THz corresponds to a frequency 10^{12} Hz, a wavelength of 300 μm (0.3 mm) and to a wavenumber of 33 cm^{-1} as it can be seen from the Table 1. In addition, terahertz wavelengths extend from 3mm (0.1 THz) up to 30 μm (10 THz). The THz field has the advantage of being within reach of both electronics and photonics technologies. Both electronic and photonic techniques can be employed in generation and detection of terahertz waves and this results in requiring the researcher to have a comprehensive understanding in both.

The history of THz waves can be traced back to the developments of the first millimeter and submillimeter wave generation and detection in 1890. Hertz first had performed experiments confirming Maxwell's theory observing wavelengths in the centimeter range [2].

Table 1.1: Electromagnetic Spectrum

	ELECTRONICS			**PHOTONICS**			
	Microwaves	mmwaves	Terahertz	Infrared	Visible	Ultraviolet	X-ray
Frequency	10 GHz	100 GHz	1 THz	10 THz	100 THz	10000 THz	10^6 THz
Wavelength (mm)	30	3	0.3	0.03	0.003	$3x10^{-5}$	$3x10^{-7}$
Wave number (cm^{-1})	0.33	3.3	33	333	3333	333333	33333333
Energy	$4.1x10^{-5}$ (eV)	$4.1x10^{-4}$ (eV)	$4.1x10^{-3}$ (eV)	$4.1x10^{-2}$ (eV)	$4.1x10^{-1}$ (eV)	$4.1x10^{1}$ (eV)	$4.1x10^{3}$ (eV)
	$6.6x10^{-24}$ J	$6.6x10^{-23}$ J	$6.6x10^{-22}$ J	$6.6x10^{-21}$ J	$6.6x10^{-20}$ J	$6.6x10^{-18}$ J	$6.6x10^{-16}$ J

At the end of the 19th century Rubens published many articles exploring his own work in the far-infrared region, he extended the spectrum from centimeter range to approximately 20 μm. Then, even more research had been carried out in the field of far-infrared, between 1920 and 1930 some 40 FIR papers were published and from 1930–1940 another 80 [3]. After the World War 2, the first studies on molecular spectra with coherent THz radiation were carried out [2]. In addition, remarkable resolution was achieved enabling precise determination of molecular sizes and shapes. During 1950's by the invention of more sensitive detectors, even more important developments in Far Infrared Spectroscopy had been achieved. In the early 1960's the invention of the laser contributed to the revolution in far-infrared region. Many of the far-infrared instruments used today were developed in that period. During the 1970's, development in the fields of both the millimeter and submillimeter has continued [2]. Terahertz optoelectronics was further advanced with the invention of short optical pulses and the development of the ultrafast photoconductive (PC) thin films. Novel techniques developed by Auston in 1980 [4] accelerated the research in THz region. In 1984, Auston, Cheung and Smith reported

emission and detection of approximately 1.6 ps long electromagnetic (EM) pulses using a PC switch which is positioned symmetrically on opposite sides of a dielectric slab [5]. Ultrafast transient current in the photoconductive switch was the source of the THz radiation and coherent sampling of electromagnetic pulses was used as the detection method [6]. In 1988, Smith, Auston and Nuss published their work in which an antenna is used both as an emitter and detector and they showed that THz waves are also observed as electromagnetic transients emitted from the PC antenna [7]. Later, complete terahertz time-domain systems which can be used in spectroscopy were developed. Achievement in the generation of sub-100 fs optical pulses by using self-mode-locked operation in Ti:sapphire oscillators and achievements in obtaining shorter carrier lifetime while keeping mobility high had accelerated the development of THz systems in early 1990's [5]. Apart from the developments in the PC antenna, in the beginning of the 1970s, generation in the THz frequency range due to another process: optical rectification was reported by two groups, Yajima and Takeuchi and Yang [8], as well as Richards and Shen independently [5]. Generation of THz pulses by optical rectification is widely used as it emits a broader radiation than PC methods [9]. And instead of PC detection, electro-optic detection has also developed as a successful tool for detection of THz pulsed radiation [10]. As early as 1985, Auston et al. detected Cherenkov shock waves as a result of transient nonlinear second order polarization using the electro-optic (EO) effect [11]. In 1995, Wu and Zhang detected freely propagating electromagnetic radiation with subpicosecond resolution by using EO effect [12]. This application is based on the linear electro-optic effect (Pockels effect) and it offers ultrawide bandwidth detection.

These waves and their applications are studied in many different ways. First of all, the frequency range in the terahertz is very unique and important because it shows different characteristics for different materials. For instance, THz fields interact strongly with polar substances but penetrate those that are non-polar. Thus, different polar elements (molecules with a net dipole moment) have different spectral peaks in the THz range which makes gas sensing possible in this range. Secondly, another application of THz is in investigating biological substances due to the fact

that some of them have distinct fingerprints in the THz range (the mechanism of absorption of the terahertz frequency here is generally due to torsional-vibrational modes in the biological molecule) [5, 9]. Thirdly, in terms of electronics terahertz can also mean carrying information in the 1-10 Tb/s range for optical communication systems. In addition, computers with ultrafast speed could be achievable by using 1 ps switching performance of a THz transistor [9].

On a different note, experimental studies of the spectral energy distributions in observable galaxies show that approximately one-half of the total luminosity and 98% of the photons emitted since the Big Bang fall into the submillimeter and far-IR [13].

Imaging is another area of terahertz studies. It is possible to image plastic explosives for security reasons [14], as well as biomedical imaging [15], cancer tissues [16], chips [1], and semiconductor wafers [17]. Another application of THz waves is in electrical characterization of conductors. Carrier dynamics of semiconductors [1, 12], and dielectric constant measurement of thin films [18] are two examples of THz spectroscopy.

Finally, THz waves can be used to investigate plasma. For most laboratory generated plasmas terahertz allows the ability to span the spectrum above and below the plasma frequency. This makes THz spectroscopy a non-contact tool compared to other methods. Another way to state this is that the broad bandwidth of a THz pulse spans both above and below the plasma frequency allowing us to extract information about the complex susceptibility of the plasma [19]. Further, plasma is the collection of neutral and ionized particles which contains approximately equal amount of negatively and positively charged particles. For standard laboratory plasmas with electron densities in the range $10^8\ \mathrm{cm}^{-3} \leq n_e \leq 10^{14}\ \mathrm{cm}^{-3}$, the plasma frequency lies in the range $90\ \mathrm{MHz} \leq f_p \leq 90\ \mathrm{GHz}$ [20]. Plasma is transparent above plasma frequency and it is opaque below. To understand the plasma density it is therefore important to operate at frequencies closer to the plasma frequency. Time dependent plasma diagnostics is possible due to the short pulse duration (ps) allowing for a large range of density fluctuations to be detectable due to the large frequency range of a typical THz pulse [19]. In this thesis we will concentrate on studying laboratory generated

plasmas using terahertz time-domain spectroscopy. We will try to understand the interaction of a DC electrical discharge generated plasma with pulsed terahertz waves and interpret the results to comment on some characteristics of the plasma. The structure of this work is composed of 6 parts. In the second chapter the basic principles of THz-TDS is described. Chapter 3 provides information about plasma in general, glow discharge plasmas and plasma electrodynamics. Our experimental set up is introduced in chapter 4. Next, our experimental results are stated and discussed in chapter 5 and in the final chapter the whole study is summarized.

CHAPTER 2

PRINCIPLES OF TERAHERTZ SPECTROSCOPY

The difficulty in generation and detection of coherent THz radiation has been overcome with the development of ultrafast lasers and ultrafast applications since the late 1980s. It is well known from Maxwell's equations in time domain that changing magnetic field and electric field are sources of time dependent electric and magnetic field respectively. Obviously, we may infer that any process that can cause a time-dependent change in the material properties such as the polarizability or change in conductivity will result in emission of radiation. This is simply the basic mechanism of THz generation. THz detection methods also make use of the advantages offered by ultrafast optics. In this chapter, THz generation using resonant and nonresonant methods will be explained, and then the two most common pulsed THz detection methods based on photoconductive (PC) sampling and electro-optic (EO) sampling will be discussed. Finally Terahertz Time-Domain Spectroscopy (THz-TDS) systems will be introduced.

2.1. Terahertz Generation

Employing ultrafast optical pulses is one of the most common techniques amongst researchers to generate and detect THz pulses. This technique can be grouped in to two; resonant techniques and nonresonant techniques [15]. In resonant techniques, photon absorbed by a photoconductor causes creation of electron-hole pairs that leads to THz generation. On the other hand, non resonant techniques rely on nonlinear optical effects.

2.1.1 Photoconductive Antenna

The oldest method used to generate and detect terahertz radiation is photoconductive antennas and they will be discussed in this section. The main advantage of this method is the very high efficiency in conversion ultrafast visible laser power to THz laser power compared to other techniques such as optical rectification [21]. Here, an induced conductivity change in a photoconductor triggered by an ultrafast laser pulse generates terahertz radiation. This method has gained use after the development of ultrafast optical techniques since the late 1980's. The main reason behind the need of ultrafast lasers is that ultrafast optical pulses generate corresponding ultrashort electrical pulses (depending on the speed of the electrical medium). In other words, operation with ultrafast optoelectronic materials requires ultrafast optical pulses. Ultrafast switching and gating in a photoconductor driven by ultrashort laser pulses was demonstrated first by Auston [4]. Auston et al. demonstrated this by employing photoconductors in specific antenna geometry, namely, elementary Hertzian dipoles were used for both transmitting and receiving antennas [7]. A Hertzian dipole structure means the current element much smaller than the wavelength [22] i.e. it is an infinitesimal dipole [5].

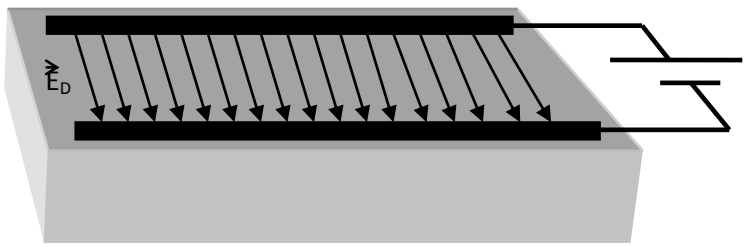

Figure 2.1: Illustration of a basic photoconductive switch

In Figure 2.1, a simple schematic representation of an antenna is shown. Basically it consists of a semiconductor substrate and two parallel metal lines deposited on it. As it shown a bias voltage is applied to these lines to create an electric field in the gap. Absorption in the photoconductor limits the generation of

THz radiation only to near surface. From the schematic of the system, it is precise that it could be considered as a parallel plate capacitor that stores energy. Emission of THz radiation from this system can be thought as shorting a capacitor by exciting the gap with an optical pulse. Hence, a femtosecond laser pulse initiates the physical process of emission. Following this, the photons having energies greater than the band gap of semiconductor are absorbed as seen in figure 2.2.

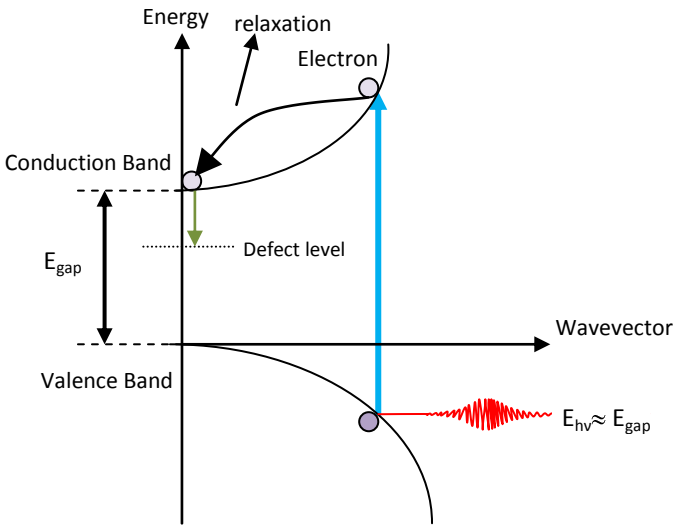

Figure 2.2: THz generation by photon absorption

Then, photon absorption leads to the creation of electron-hole pairs in the photoconductor that can be considered as electron-hole plasma. The plasma is initially electrically neutral because of the fact that one absorbed photon creates one electron and one hole. In addition, the change in charge density is proportional to the intensity of the optical pulse. Next, the carriers are accelerated in the electric field. Electrons move toward the positive line whereas holes move in the opposite direction, i.e. towards the negative one. Additionally, charge separation creates electric field in the gap in the opposite direction so the field is reduced which decreases the force on the carriers in turn. The conduction current in the material is given by J(t) = N(t).*e*.v(t) where N(t) is the carrier density, e is the charge and v(t) is the velocity of carriers. Time dependence of the velocity is based on the fact that the carriers are initially at rest and accelerated by the electric field. Then, a time dependent polarization P(t) is induced due to the charge separation. Here polarization

is defined as P(t) = N(t)*e*r(t) where r is the distance between charges. In brief, we will consider this system as a simple dipole for better comprehension. The emitted time dependent electric field of an elementary Hertzian dipole antenna in free space is described as;

$$\vec{E}(\vec{r},t) = \frac{l_e}{4\pi\varepsilon_0 c^2 r}\frac{\partial \mathcal{J}(t)}{\partial t}\sin\theta \;\propto \frac{\partial \mathcal{J}(t)}{\partial t} \tag{2.1}$$

where J(t) is the current in the dipole, l_e the effective length of the dipole, ε_0 the dielectric constant of a vacuum, c the velocity of light in a vacuum, and θ the angle from the direction of the dipole [5].

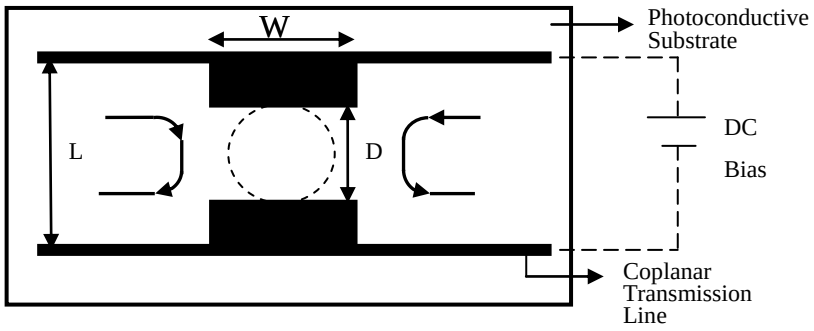

Figure 2.3: Basic Hertzian Dipole

From the equation above dependency of amplitude to the antenna length could be seen. Under the same bias and pump conditions, there is no significant difference is observed in the frequency domain however longer antennas yield larger signal amplitudes as expected from Eq. 2.1, so, longer antenna length increases the emission power as expected [23]. Moreover, there is a direct relation between the emitted power with bias voltage and incident laser power because of the direct proportionality of photocurrent both bias and pump power. Thus the limiting factor for maximizing radiation power with increasing bias and pump power is definitely the breakdown voltage of the photoconductor. High resistivity substrate is a necessity to apply high bias. This time the difficulty arises from the fact that high resistivity substances own low mobility, which decreases the emission efficiency of antenna. At this point, we need to consider that short carrier lifetime is not essential for the emission efficiency but high resistivity is so [17]. Thus, materials with high resistivity and moderate carrier mobility perform better. An additional discussion is

the bandwidth of the antenna. Duvillaret et al [24] stated that the laser pulse duration is the most important parameter to enhance the emitted THz signal. Also, Tani et al [17] claim that generation and detection bandwidth can be expanded by using short enough laser pulses.

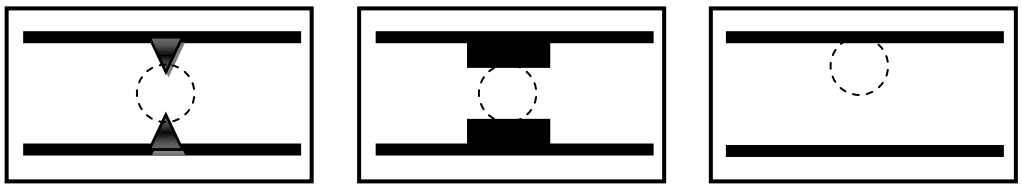

Figure 2.4: Types of antenna (a) bowtie antenna (b) dipole antenna (c) coplanar stripline

There have been several kinds of antenna structures developed and some kinds of them could be seen in Figure 2.4. The first one in the figure is a bowtie antenna. In addition, the pulse emitted from the bowtie antenna is broader than the one emitted from photoconductive dipole antenna under similar bias and pump-power conditions and the frequency spectrum of the bowtie extends to lower frequencies than the dipole [25]. Thereto, stronger signal amplitudes are observed by the bowtie antennas compared to the dipole antennas [23]. The basic structure of the dipole antenna can be seen in Figure 2.3. It consists of a photoconductive gap located in the middle of a coplanar transmission line and a semiconductor substrate with a short carrier lifetime as stated earlier. The typical size of the PC gap D is 5–10μm, width W is 10–20 μm and length L is 30–50 μm for a Hertzian dipole antenna [17]. The resonant frequency of a dipole antenna can be approximated as

$$\nu_r = \frac{c}{\lambda_r} = \frac{c}{2l_e\varepsilon_e^{1/2}} \tag{2.2}$$

where λ_r is the resonance wavelength, ε_e is the effective dielectric constant and l_e is the effective length of the antenna [23].

The requirements for THz generation are given as follows. First of all, the process of generation of electron hole pairs in a semiconductor as a result of photon absorption is a fast process so the duration of both optical and electrical pulses should be nearly identical. Another important point is that the semiconductor

bandgap energy needs to be smaller than the photon energy to allow the incoming photons to be absorbed. Also, material should have low carrier lifetime but high mobility. However, there is an inverse relationship between them, so the system should be optimized. In addition, the area of the gap between the transmission lines is another factor that determines the sensitivity of the material since minimizing the capacitance of the gap minimizes the response time. Another factor that affects the speed and sensitivity is the optical pulse duration that excites the photoconductor.

The materials that are used as a photoconductor are generally GaAs and LT-GaAs. The characteristics of some materials used are given in Table 2.1. The usage of them does not have a long story. It begins with the use of radiation-damaged Si-on-sapphire (RD-SOS) as a fast response photoconductor by Smith et al in 1981.

Table 2.1: Characteristics of photoconductive materials

Photoconductive Materials	**Carrier Lifetime (ps)**	**Mobility ($cm^2/(V.s)$)**	**Resistivity (Ω.cm)**	**Band Gap (eV)**
Cr:doped SI-GaAs	50 - 100.0	≈ 1000	10^7	1.43
LT-GaAs	0.3	150 - 200	10^6 (5×10^5)	1.43
SI-InP	50 - 100.0	≈ 1000	4×10^7	1.34
Ion-Implanted InP	2 - 4.0	200	≈ 10^6	1.34
RD-SOS	0.6	30		1.10
Amorphous Si	0.8 – 20.0	1	10^7	1.10
MOCVD CdTe	0.5	180		1.49
LT-$In_{0.52}Al_{0.48}As$	0.4	5		1.45
Ion-implanted Ge	0.6	100		0.66

In 1990, Grischkowsky et al [26] showed that GaAs leads to a broader spectrum and larger signal amplitude compared to RD-SOS. Then, for the reason that

GaAs has high optical and electrical quality as a PC material, it reached a widespread use. Therefore, antenna structures fabricated on GaAs substrate have been used commonly as an emitter or detector. Further, LT-GaAs is advantageous to have the highest possible mobility with the shortest possible carrier lifetime [27]. On the other hand, antennas fabricated on SI-GaAs rather than LT-GaAs used more frequently because of the enhanced emission power. In addition, this enhancement is attributed to the higher mobility of the carriers on SI-GaAs than that of in LT-GaAs [5].

Furthermore, a hemispherical silicon lens where the flat side is attached to the antenna is used to reduce the reflection loss at the air–substrate interface and to collimate the beam by locating the emitter at the focus of the substrate lens. Position of the lens can be seen in Figure 2.5 and focusing in the presence of the lens in Figure 2.6. Having very low absorption and nearly uniform index of refraction, silicon is the most suitable material for this purpose [28]. Moreover, the collimating lens has no effect on the bandwidth of the radiated terahertz pulse.

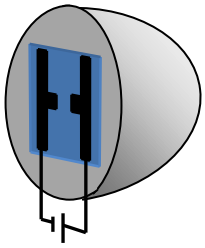

Figure 2.5: Antenna mounted on a hemispherical silicon lens

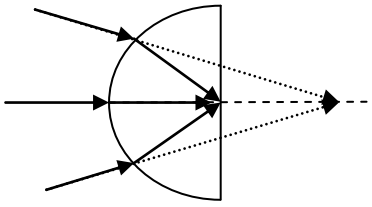

Figure 2.6: Illustration of beam collimation by hemispherical silicon lens.

2.2.1 Optical Rectification

In the previous part THz generation via induced polarization by photon absorption is discussed. In this chapter, we will discuss completely different phenomena from the previous. The former method is resonant but the latter is nonresonant which means that no photon absorption occurs. The interaction between nonlinear crystals with electric field of an ultrashort pulse is the physical mechanism behind. In other words, optical rectification is creation of pulsed radiation in the THz range as a result of this interaction. It was first reported in the beginning of 1970 that by using a second order nonlinear crystal and picoseconds pulses; far-infrared radiation due to optical rectification was observed [5]. Then, Hu et al. produced radiation with a bandwidth of 1 THz by optical rectification of femtosecond laser pulses in LiNbO3 in 1990 [8]. Finally, electro-optic sampling of freely propagating THz-radiation pulses was demonstrated in 1995 by Wu and Zhang [5] and in 1996 by Jepsen et al. and Nahata et al [8].

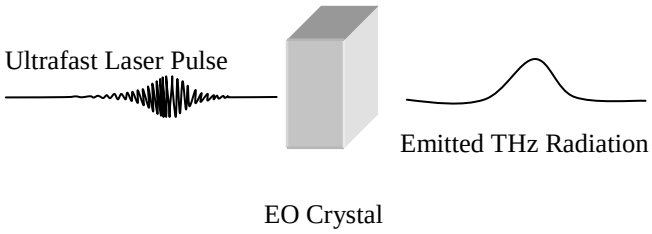

Figure 2.7: Illustration of optical rectification (the generated pulse is the envelope of the optical pulse [29])

The basic physical principle behind is the emitted terahertz field is proportional to the second-order time derivative of the second-order polarization. In a linear material, incident pulse induces polarization in the direction of the electric field of the pulse. On the other hand, response of nonlinear materials is different. The polarization induced in the material is:

$$\vec{P}(t) = \chi^{(1)}(t)\vec{E}(t) + \chi^{(2)}(t)\vec{E}(t)\vec{E}(t) + \chi^{(3)}(t)\vec{E}(t)\vec{E}(t)\vec{E}(t) + \cdots \quad (2.3)$$

where χ is the electric susceptibility [22]. In addition, the second order susceptibility $\chi^{(2)}$ is the main term in emission of THz pulse i.e. $P^{(2)}=\chi^{(2)}.E^2$. Here, polarization could be thought as in the previous chapter but the charge separation is smaller due to the fact that electrons are not free. The time domain terahertz profile is gives by $E_{THz} = \frac{\partial^2 P(t)}{\partial t^2}$.

To having a better understanding of optical rectification, it would be better to work in frequency domain. If an optical pulse having an oscillating electric field incident to a crystal having nonlinear optical properties, it gives rise to an oscillating polarization in the crystal. As an example, if we have two fields having frequencies ω_1 and ω_2 respectively, the induced polarization consists of two parts depending on $(\omega_1 + \omega_2)$ and $(\omega_1 - \omega_2)$. Emission of THz radiation by nonlinear effect based on ω_1-ω_2, i.e. difference frequency generation. Likewise, if a laser pulse having bandwidth $\Delta\omega$ is incident to a crystal, we need to consider all difference frequencies within the bandwidth of the pulse. Therefore, bandwidth of the radiated THz pulse is determined by the bandwidth of the ultrashort pulse.

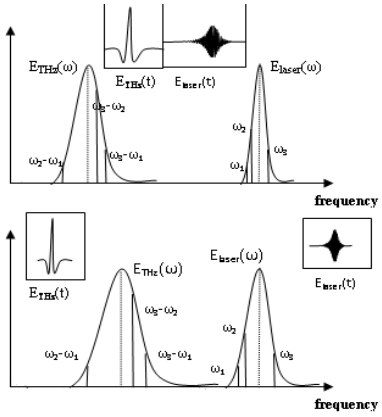

Figure 2.8: Illustration oh THz generation with optical rectification for two different incident pulse [22].

In the Figure 2.8, from Mittleman, an illustration of terahertz generation by optical rectification could be seen. Three frequencies ω_1, ω_2 and ω_3 from ultrashort pulse leads to the generation of frequencies ω_2-ω_1, ω_3-ω_2, and ω_3-ω_1. The insets show

the optical and terahertz pulses in the time domain. The upper figure illustrate the THz generation for a longer optical pulse with smaller bandwidth, the lower shows for shorter optical pulse with corresponding larger bandwidth. Further, generated radiation is proportional to intensity envelope of the optical pulse, therefore it is precise that emission efficiency is sensitive to changes in both optical pulse duration and beam waist [30] i.e. beam profile of the incident pulse determines THz profile [22]. By using laser pulses with broad bandwidths i.e. short durations, THz bandwidth can be extended to higher frequencies. Also, amplitude of the terahertz pulse is proportional with the pulse energy of the laser pulses [31]. In addition, pc generation acts as a point source however optical generation doesn't. The most commonly used nonlinear crystals for generation are ZnTe, GaP and GaSe with large bandgap [32]. Despite the low emission power [33], optical rectification attracts much attention for its simplicity and extended bandwidth to higher frequencies [5].

In this part of the discussion, we will continue with the efficiency in terahertz generation from optical rectification. First, the material needs to be transparent for both THz and optical radiation to allow the generation takes place in the entire path. However, because of the wavelength dependency of refractive indices, velocity of terahertz pulse and laser pulse are different. To improve efficiency velocity difference should be as small as possible. Thus, phase matching condition is important to maximize the efficiency by allowing greater interaction between terahertz and optical pulse. So, they should be in phase during the whole interaction length. To achieve this condition, phase of the THz wave travels at the velocity of the optical pulse envelope i.e., the optical group velocity, v_g [34, 35]. Further, the length that the difference can be ignorable for generation is called coherence length. So, it is enough to keep the crystal length shorter than the coherence length. However, crystal thickness has some other effects in efficiency. For instance, broad bandwidth and short pulse requires thinner crystals but thick crystal increase the strength of emission power [33, 31]. One another limitation is the absorption in the nonlinear material which constraint the bandwidth of the THz pulse.

2.2. Terahertz Detection

Once the THz pulse is emitted, the shape of its electric field can be determined through several methods but two of them are commonly used. In contrast to many optical methods, where only the light intensity is measured, terahertz detection methods allow to get information about both amplitude and phase. However, THz detection is difficult because of the low emission power of THz pulse. Generally, coherent detectors are necessary to detect pulsed terahertz radiation for time domain spectroscopy systems. Photoconductive detection and electro-optic detection are the two most common methods where both of them require to employ ultrafast electromagnetic pulses. Basically, for pc detection an identical antenna structure to the pc emitter may be used without applying a bias voltage. Furthermore, electro optic detection is a coupling between THz pulse and optical pulse in the sensor crystal. In addition, detection bandwidth of electro-optic crystals is huge compared to the limited bandwidth of photoconductive antenna but pc antennas are extremely sensitive [5, 9, 35].

2.2.1. Photoconductive Detection

Detection of THz pulses via photoconductive antenna based on the same mechanism used to generate the pulses. Similarly, rapid changes in conductivity are triggered by incident ultrafast pulse excitation in a photoconductor material i.e. by photo-induced electrons and holes. The speed and sensitivity of detection is influenced by both semiconductor properties and the geometry of antenna [36] and optical pulse duration [5, 6, 7, 8, 37, and 38]. A typical design of the antenna from front view is given in the Figure 2.9.

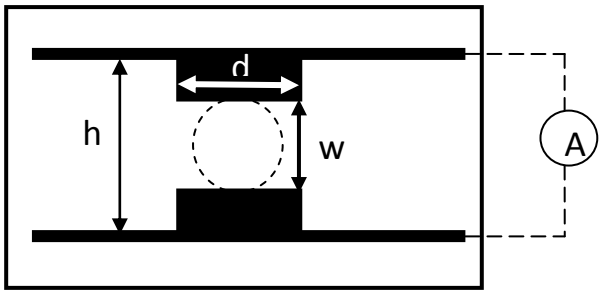

Figure 2.9: Schematic view of a typical pc antenna detector

The antenna is a dipole fabricated between coplanar strip lines with length, h, the most critical element affecting detection parameter. By connecting the lines to a highly sensitive current amplifier, current within the antenna gap can be detected with subpicoamp resolution. As the antenna is center-excited, the gap is approximated to the diameter of the focused incident laser pulse. When there is no excitation on the antenna, the dark resistance is on the order of mega ohms depending on the resistivity of the semiconductor substrate and antenna and also dimensions of coplanar stripline. Distinct from the generation case, an unbiased antenna is used to detect terahertz radiation therefore the acceleration of carriers do not have any exact direction. They are accelerated by the THz electric field. Low-temperature-grown GaAs has been the most widely used material for the PC detector because of its unique properties, such as the ultrashort carrier lifetime, large resistivity, and relatively good carrier mobility [17, 38].

Ignoring the negligible contribution from metal lines [36], resistance of the antenna is determined by the antenna gap given by the formula $R=w/\sigma(t)A$ where A is the cross-sectional area [22, 8]. Here, A could be approximated $2d\alpha$ where d is the gap width and α is the absorption depth in the semiconductor. Incidence of the laser pulse on the photoconductor could be thought as closing a switch because of the fact that it allows the antenna gap to conduct. So, the gap resistance change from nearly insulating to conducting and then get back to insulating on a short time scale due to the short recombination time of carriers, i.e. closing and opening the switch simultaneously. The voltage bias on the antenna is constructed by the electric field of the incident THz pulse which is given by $V_{BIAS}(t) = h \cdot E_{THz}(t)$. Thus, an instantaneous current is produced by the incident THz pulse in the antenna which is determined from Ohm's law as $I_{THz}(t) = E_{THz}(t) \cdot h \cdot 2d\alpha\sigma(t)/w$ [22, 8]. Because the conduction in the antenna is formed for an instant of time, the current is proportional to the THz electric field. Then, time averaged current is measured. Additionally, the shorter the carrier life time, more sensitive the detector permitting the measurement of more rapidly changing THz field transients.

In Figure 2.10, illustration of the process of measuring the time dependent electric field of a THz pulse is given.

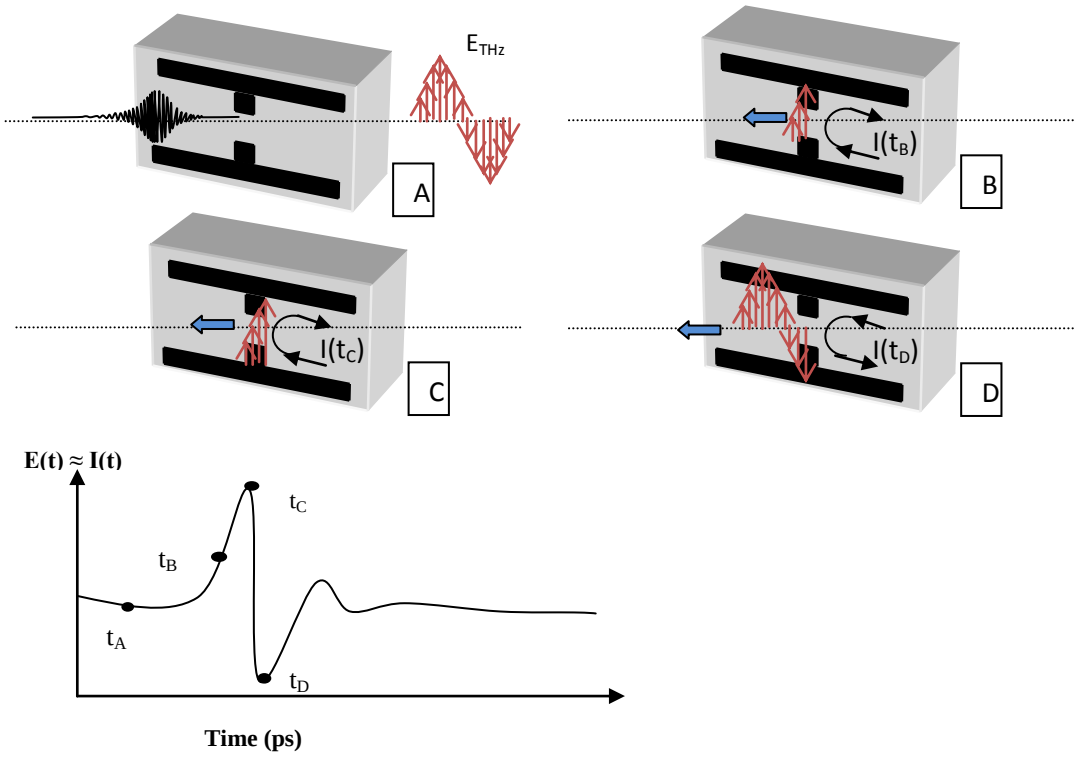

Figure 2.10: A figure illustrating the measurement of THz pulse using photoconductive sampling: The bottom frame shows the corresponding measured THz waveform, with four specific frame is marked [22].

First, a focused ultrashort laser pulse excites the gap in the antenna structure from left hand side. From right hand side, THz pulse travels through the antenna. To preserve timing, pump and probe pulse are the ones that are splitted into two from the same laser pulse. In the first frame (a) the average current which flows through the antenna is zero since the THz pulse has not arrived yet so no electric field. In frame (b) the delay between the pump and probe pulse has been changed so that the front of the THz pulse and gating pulse arrived to antenna at the same time. Measurement is done by keeping the position constant while the current has been measured. After, the delay is again changed to measure the next point on the pulse. Frames (c) and (d) show measurements at different positions of the THz electric field respectively. The shape of the THz pulse is obtained by incrementally changing the delay. At the bottom figure, measured waveform at given points is represented.

2.2.2. Electro-optic Detection

Electro-optic effect can be considered as the inverse of optical rectification, in which an applied electric field to an electro-optic crystal leads to a change of the refractive index, namely "The Pockels effect". It is based on the measurement of phase modulation induced in the electro-optic crystal in order to extract terahertz waveform. The basic detection configuration for electro optic detection is shown in Figure 2.10 from Mittleman. In order to detect THz pulse, careful alignment of THz pulse and the probe pulse is needed because they both should copropagate along the same axis. If we assume that the pulses propagate in z direction, probe beam is polarized along y direction by locating a polarizer. When the terahertz beam illuminates the crystal, index of refraction is modulated. The induced change of refraction by THz electric field is probed by a femtosecond optical pulse through the crystal. After, modulated birefringence leads to a rotation of the electric field vector of the laser pulse, with an angle proportional to the applied field i.e. polarization of optical probe beam changes. Following the EO crystal there is a quarter wave plate and then a Wollaston prism. A quarter wave plate changes linearly polarized light to circular or vice versa and a Wollaston prism splits light into two orthogonal, linearly polarized beams. THz waveform can be acquired by changing the delay. If the probe and THz pulse do not overlap in the crystal, birefringence is not created. Thus, optical pulse polarization does not chance. Thus, optical pulse would be circularly polarized after the wave plate, i.e. equal electric field components along both the x and y axes. The Wollaston prism splits the optical beam into x and y components of polarizations. Then, two photodiode detect each polarized component separately. Difference between the intensities of the x and y polarized components gives rise to a current which is detected by a lock-in amplifier. Figure 11 displays visualization of THz generation by optical rectification in detail. In the first figure, since there is no birefringence along the crystal, intensities of the polarized components are equal; hence no signal is detected from the photodiodes. In the second figure, the probe is delayed and then the electric field of the pulse overlaps with the negative electric field of the THz pulse. As a result, birefringence is induced which changes the

polarization of the optical probe pulse. Following the copropagation of the pulses through the crystal, optical polarization has been a little rotated.

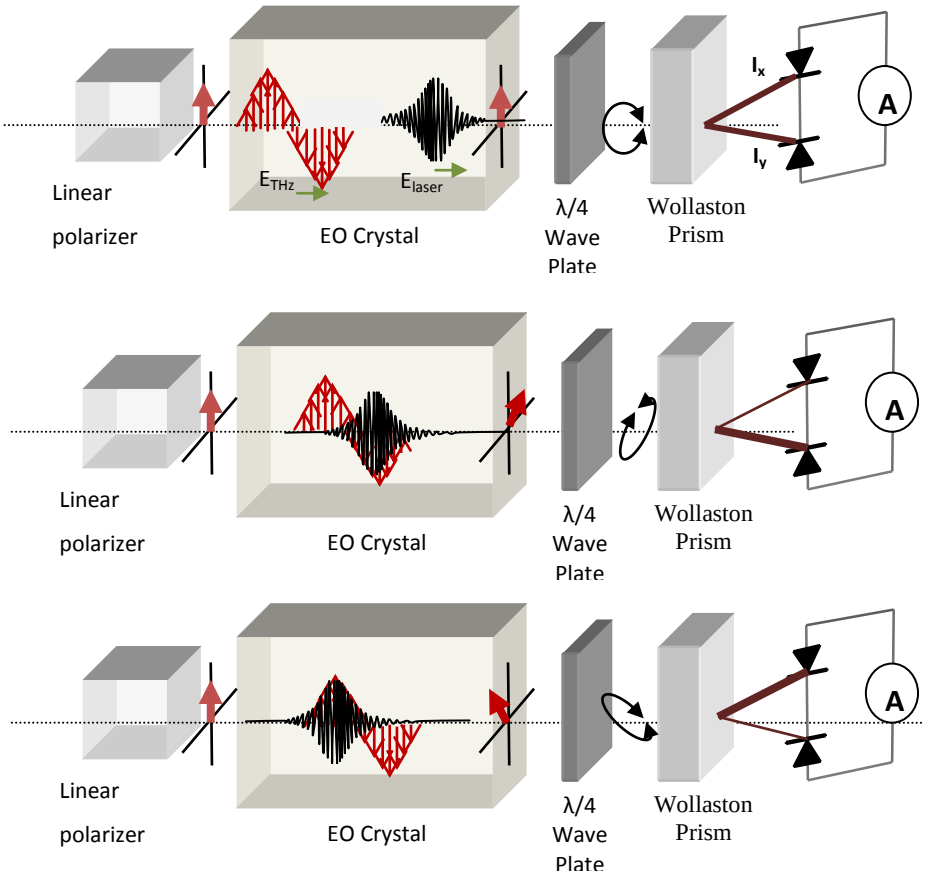

Figure 2.11: Detection by electro-optic sampling [22].

Then, elliptical polarization is obtained after the quarter wave plate. Next, the beam is incident to the Wollastan Prism which separates it to its components having different intensities. Due to the difference in the intensities, a signal is detected by photodiodes. In the third figure, the timing is again changed allowing electric field of the optical pulse and the positive electric field of the THz pulse overlaps. The change in polarization is now in the opposite direction which gives rise to a signal in the photodiodes in reverse direction. The time dependent waveform of the THz radiation can be obtained by changing the relative delay between the laser and terahertz pulses.

Since Pockels Effect is the reverse of optical rectification, factors limiting the terahertz generation by using electro-optic crystals also limit electro-optic detection. As an example, to increase detection sensitivity, longer electro-optic crystals may be used as the induced phase change is proportional to the length of the crystal.

Nonetheless, longer crystal increases the THz absorption and effects phase mismatch between the optical pulse and THz pulse. This can be handled by using thin crystals which in turn decrease the sensitivity. In addition, as in the case of electro-optic generation, coherence length is also applicable to detection which means that thinner crystals allow broadband detection. Moreover, frequency bandwidth of the measurement is also affected by the duration of the ultrafast laser pulse. In order to increase the sensitivity, shorter laser pulses should be used.

A variety of electro-optic materials have been used for EO detection. First, in 1995 Zhang and Wu reported detection of terahertz pulses by using $LiTaO_3$ [10]. Then, they demonstrated use of ZnTe but the efficiency of ZnTe is limited by the large group velocity mismatch between THz and optical pulse [39]. GaP is an excellent alternative to ZnTe for electro-optic detection but the electro-optic coefficient of GaP is one fourth that of ZnTe [8]. In 1997, the same group showed detection of THz radiation by using a GaP crystal [40]. One another electro-optic crystal used for detection is ZnSe with electro-optic coefficient is half of the ZnTe [8]. Table 3 shows some characteristics of electro-optic crystals used for detection.

Table 2.2: Properties of Typical Electro-optic Sensor Crystals [8]

Material	**Crystal Structure**	**Electrooptic Coefficient (pm/V)**	**Group Velocity Mismatch (ps/mm)**	**Surface Orientation**	**Experimental Detection Bandwidth (THz)**
ZnTe	Zincblende	r_{41}=3.90	1.1	110	2.5
GaP	Zincblende	r_{41}=0.97	-	110	7
ZnSe	Zincblende	r_{41}=2.00	0.96	111	3
$LiTaO_3$	Trigonal	r_{33}=30.3	14.1	-	-
GaSe	Hexagonal	r_{22}=14.4	0.10	-	140

2.3 Terahertz Time Domain Spectroscopy

One of the most common applications of THz waves is spectroscopic measurements. A large number of variations of spectroscopic techniques have been developed like Terahertz Time Domain Reflection Spectroscopy, THz Emission Spectroscopy, Optical Pump-THz probe Spectroscopy, Terahertz Time-Resolved Spectroscopy and Terahertz Time Domain Transmission Spectroscopy. Among them THz Time Domain Transmission Spectroscopy will be discussed in this part of the chapter in terms of brief description of THz spectroscopy and process to extract spectroscopic information from measurements of THz pulses. From now on Terahertz Time Domain Transmission Spectroscopy will be used as THz-TDS in short. As already stated in the first chapter, THz spectral region lies between 0.1 THz to 10 THz. Besides, above 10 THz, optical spectroscopy techniques are more effective, and below 0.1 THz, electronic techniques are more effective. THz-TDS measures the electric field of the freely propagating pulse and it offers extracting both real and imaginary parts of the refractive index along the propagation path. For spectroscopy, the same ultrafast laser pulse is used both for generation and detection of the THz to guarantee precise timing between optical pump pulse and gating probe pulse. A typical set up for THz-TDS is given in Figure 12. The collimated THz beam between the off-axis parabolic mirrors passes through a sample which is to be characterized. By investigating the change of time dependent electric field due to the interaction between pulse and sample, spectroscopic information is provided.

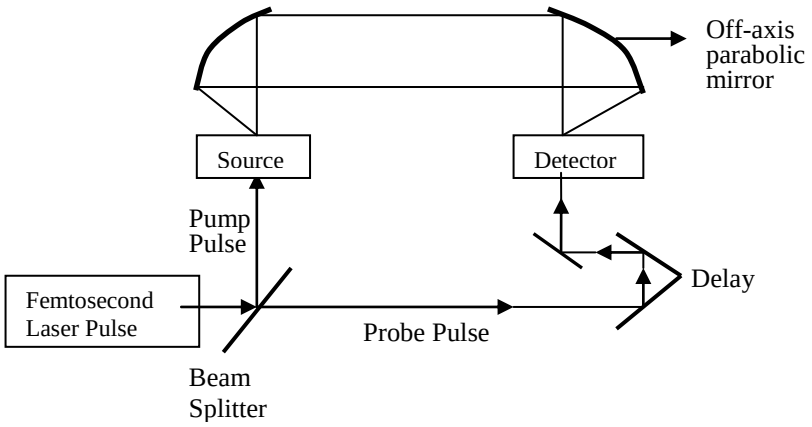

Figure 2.12: Typical set up for THz-TDS

To obtain spectroscopic information, time domain pulse are represented in the frequency domain as a superposition of plane waves of frequency ω, all with a k vector along the THz system optical axis, z. Then, in order to find the relative amplitude and phase of each plane wave component of the THz pulse, Fourier transform is used to get

$$E(\omega) = |E(\omega)|e^{i\varphi(\omega)} \tag{2.4}$$

where |E(ω)| is the THz field amplitude and φ(ω) is the phase of the electric field. To extract information from THz systems, measurements with and without a sample should be compared to obtain complex refractive index. It should be noted here that any possible reflection at the surface of the sample is ignored. An additional assumption is that during the measurements with and without sample, characteristics of THz pulse are not chance. Therefore, measurements need to be done under steady conditions meaning avoiding long duration experiments. Assume that two measurements with and without sample gives us the Fourier transformed data $E(\omega) = |E(\omega,0)|e^{i\varphi(\omega,0)}$ and $E(\omega,l) = |E(\omega,l)|e^{i\varphi(\omega,l)}$ respectively where l is the length of the sample. To get complex refractive index $n(\omega) = \eta - i\kappa$, we will make use of phase information to obtain real part and amplitude information to obtain imaginary part by using the following relations. In the index equation, sign of the imaginary part is taken to be negative to represent attenuation. First, real part of the index is given by

$$\eta(\omega) = \frac{1}{kl}\big(\varphi(\omega,l) - \varphi(\omega,0)\big) \tag{2.5}$$

where k is the wave vector of the terahertz pulse. Second, imaginary part of the index is given by

$$\kappa(\omega) = \frac{1}{kl}\left(ln\left(\frac{E(\omega,l)}{E(\omega,0)}\right)\right) \tag{2.6}$$

From this point, we may find the absorption coefficient by using the relation $\alpha(\omega) = \frac{2\omega\kappa}{c}$ where c is the speed of light. Also, dielectric function could be found by using $\varepsilon(\omega) = (n(\omega))^2$. Additionally, transmission spectrum can be obtained by taking the ratio of the power with and without the sample $T = \left|\frac{E(\omega,l)}{E(\omega,0)}\right|^2$. To

conclude, measurement of complex refractive index is straightforward and simple in THz-TDS without needing to carry out Kramers-Kronig relations.

Next, we will keep on with two commonly used spectroscopic arrangement, Photoconductive sampling and Electro-optic Sampling. PC Sampling and Electro-optic Sampling are both gated and coherent techniques. In addition, when an ultrafast optical pulse is employed to open and close the detector (i.e. as a gate), the technique is called gated detection.

2.3.1 Photoconductive Sampling

In this part, we will explore a typical Photoconductive Sampling set up where both pc generation and detection is used. In figure 2.13, there is an experimental set up given as an example. As it can be seen from the figure above, an ultrashort laser pulse is separated into two beams with a beam splitter. The left hand side is the generation arm and the right hand side is the detection arm. Further, in order to make terahertz pulse and optical probe pulse arrive to the detection antenna together, optical path lengths of both sides should be the same. In the generation side, the femtosecond pump pulses are focused by an objective lens on the gap of the photoconductive antenna. Laser pulse excites the carriers in the photoconductor. The antenna is biased by applying voltage across the lines to accelerate the carriers. The polarization of the THz pulse is determined by the direction of the applied electric field. In addition, a function generator is connected to the generator antenna to modulate the phase. It is needed in order to provide a reference phase for the lock-in amplifier.

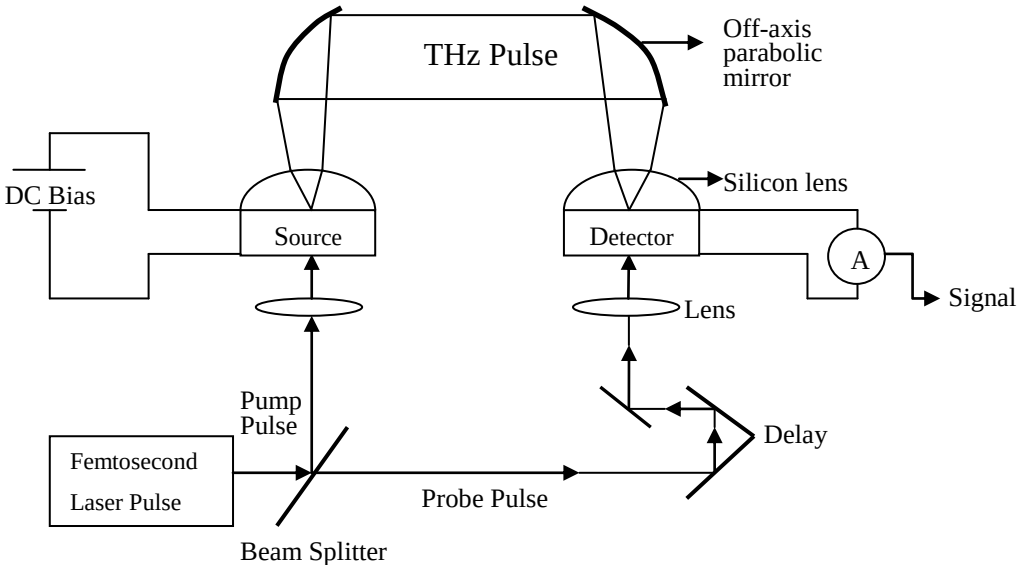

Figure 2.13: A typical pc sampling set up

Then, the generated terahertz pulse is radiated into air through a silicon hemispherical substrate lens which is mounted on the flat side to the back of the photoconductive substrate of the antenna in order to decrease reflection and refraction loss at the air–photoconductor interface and to increase the radiation efficiency. Next, an off-axis parabolic mirror is placed in front of the antenna by considering antenna is at the focus of the mirror in order to obtain a well collimated circular beam. Then, another off-axis parabolic mirror is placed exactly opposite to the previous one at the detection side. Here, a photoconductive antenna mounted on the back of a hemispherical lens with the same diameter should be in the focus of the mirror. The hemispherical lens is present to focus the collimated THz beam into the gap of the antenna. Unlike the generation antenna, detection antenna is not biased. The optical laser beam coming from the detection side that was separated from the pump beam by a beam splitter is directed by optical reflectors to the antenna in order to gate pc detector. A corner cube is located on an automatic translational stage to provide the time delay between the pump and a probe pulse. By moving the corner cube, relative time delay is chanced so the waveform is obtained. Afterward, to focus the probe beam in to the gap of the detection antenna, an objective is located to the front side. The photocurrent from the detection antenna was detected with a lock-in amplifier reference to a function generator modulating the pump laser or the bias on

the emitter PC antenna. Lock-in amplifier is employed since the current is usually very weak on the order of nA. Additionally, lock-in amplifier allows us to detect and measure very small AC signals. It is possible to measure accurately even when the small signal is masked by noises thousands of times larger than the main signal. It could select the signal at a specific reference frequency and phase enabling detection of both magnitude and the phase of the signal. Noise signals having frequencies other than the reference frequency are not taken into consideration thus they do not affect the measurement.

2.3.2 Electro-optic Sampling

The experimental set up for electro-optic sampling is very similar to the pc sampling as it is illustrated in the Figure 2.14. As in the pc sampling method pulses from a femtosecond laser source is split into a pump and a probe beam for the generation and the detection of the THz transients, respectively. The optical path lengths should be equal as in the pc sampling. Then, the pump beam is modulated by an optical chopper which is an electromechanical instrument that periodically interrupts a beam of light.

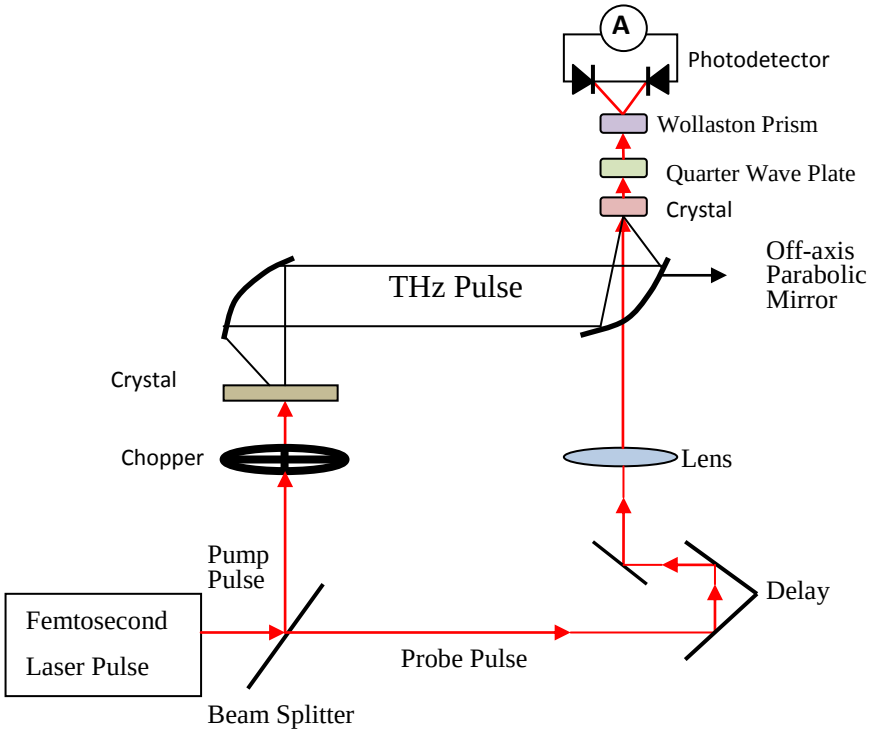

Figure 2.14: A typical set for EO Sampling.

At this time, reference signal for the lock-in amplifier is provided by the chopper located before the emitter crystal, i.e. lock-in amplifier phase-locked to an optical chopper. After, the THz radiation is emitted from the crystal according to the principle of optical rectification discussed earlier. The polarization of the emitted THz beam can be oriented by rotating the emitter crystal around the optic axis. Then, off-axis paraboloidal mirror is used to collimate the divergent beam and then by using another off-axis paraboloidal mirror placed against the first one, the terahertz beam is re-focused onto the electro-optic detection crystal. The probe pulse at the detection side is directed toward the sensor crystal by a plane mirror after passing through the corner cube. Analogous to pc sampling, the corner cube is on a translational stage to provide the relative time delay between the pump and probe pulse. On the detection crystal, incident THz pulse induces a birefringence as stated before and it causes a phase modulation in the gating probe beam proportional to the electric field of the THz pulse. In the sensor crystal, both beams need to copropagate also they need to coincident temporally and spatially. After the sensor crystal, the probe beam passes first through a quarter wave plate and then through a Wollaston prism. After all, a balanced photodetector measures the different intensities of the two polarization components.

2.3.3 Electrooptic Sampling vs Photoconductive Sampling

When we consider to sampling methods, the question “which one is more suitable for the detection of THz pulses” is coming to mind. Some studies have been carried to compare these two methods [30, 41-43]. Furthermore, two methods are more or less comparable. One of disadvantage of EO sampling is its low output power of THz pulse. The advantage of EO detection is its broad frequency range. Also, unlike the pc detection micro-fabrication facilities are not required. On the other hand, the disadvantage of pc sampling is its limited detection bandwidth. In addition, for detection between the range 0.1 to 3 THz it is found that pc antenna exhibit better signal-to-noise ratio and sensitivity when compared to electro-optic sampling for the same average THz power and low-frequency modulation [42].

CHAPTER 3

LOW TEMPERATURE PLASMA

Although materials in the form of a plasma are not widely encountered in daily life, 99% of the matter in the universe is said to be in a plasma state. Irving Langmuir used the term “plasma” in his paper in 1928 [51]. A neutral gas is ionized by applying enough energy to ionize it. Through collisions by different charged species in the plasma with neutrals, more charged particles are created. Applying an electric field to an initially neutral gas is the most commonly used technique to form plasma. For example, a few amounts of electrons or ions can be created by cosmic rays or with radioactive radiation inside a neutral gas. Applying an electric field accelerates these free charges and then new charge carriers are generated via collision processes. Plasma is defined as the collection of charged and uncharged particles in a gas which is quasi-neutral and exhibits collective behavior. So, any ionized gas cannot be thought as plasma. In this chapter, we discuss the behavior of a low-temperature plasma, namely, a DC Glow Discharge plasma. Emphasis will be given on the electrodynamics of such a medium.

3.1. Introduction

To understand plasmas we need to understand the interactions between the charged and neutral species in the plasma on a macroscopic level. In order to do so we need to discuss some basic concepts in plasma physics. First, the concept of temperature is quite different in plasma physics. The temperature and average energy of particles are closely related, $E_{av}=1/2(k_BT)$ per degree of freedom. Generally, the

unit of temperature is given in units of energy in plasma physics so that an electron temperature of 1000K actually denotes the energy of the electrons. The second concept is collective behavior of the plasma. Since there are many charged particles moving in the plasma, there may be locally placed negative and positive charges. Also movement of charges gives rise to currents creating magnetic fields. As a result, other charged particles are affected by these fields even if they are far away. Hence, collective behavior means motions that depend not only on local conditions but on the state of the plasma in remote regions as well [51]. Thirdly, a quasi-neutral plasma means that density of ions and electrons are approximately equal, i.e. plasma is electrically neutral. Next, the Debye length gives us an idea of the separation between charges. Assume that there is an isolated ion in the plasma having a potential around it. The negatively charged carriers would be attracted and positively charged carriers would be repelled by this ion. Debye length λ_D is the size of the negative charges attracted to reduce the potential to 1/e of its initial value given by the formula $\{V(r) = V_0 e^{-r/\lambda_D}\}$ where $\lambda_D = (\frac{\varepsilon_0 k_B T}{n_i e^2})^{1/2}$ and n_i is the ion density, k_B is the Boltzmann constant, ε_0 is permittivity of free space. Further, the dimensions L of the plasma should be larger than λ_D so that applied potentials are shielded out in a distance very short compared to L. Therefore, rest of the plasma does not feel the potential and free from it. Moreover, this is true if only the number of particles attracted is large enough. Hence, if $N_D = n\frac{4}{3}\pi\lambda_D^3$ gives us the number of particles in a Debye Sphere, it should be large enough to freed the rest of the plasma from the potential around the isolated ion. Otherwise, if only one or two electrons exist in the Debye Sphere, shielding concept would be statistically incorrect. An additional detail about the plasma is that the electromagnetic forces should be the dominant form affecting the gas fluid dynamics. For example, if the ionization of a gas is very weak and the collisions are resulting from typical dynamic forces, the weakly ionized gas cannot be considered as plasma as it does not show collective behavior [44]. The plasma density is characterized by electrons in the plasma oscillating around their equilibrium position with a frequency, namely the plasma frequency. Plasma frequency can be found by using the equation of motion and continuity equation for the electrons as

$$\omega_p = \left(\frac{n_e e^2}{\varepsilon_0 m_e}\right)^{1/2} \quad (3.1)$$

where n_e is the electron density, e is the charge of the electron, ε_0 is permittivity of free space and m_e is the mass of the electron (see below for the derivation). It can be approximated by the formula $\omega_p/2\pi = f_p \approx 9\sqrt{n}$ [44]. Further, $\omega_p\tau$ □1 where τ is the mean time between the collisions in order to satisfy the condition that the gas behaves as plasma rather than a neutral gas. Thus, the motion is dominated by electromagnetic forces. Additionally, plasma is called "cold" if it is weakly ionized or it is called "hot" if it is fully ionized and nearly collisionless [65].

3.2. DC Glow Discharge

The first studies on gaseous conduction were done by Coulomb in the late 18th century [55]. The investigation of glow discharge plasma systems accelerated after the discovery of electrons. Later, as higher potentials were applied to electrodes in low pressure glass tubes, colorful (visibly) glows were observed. In 1944, Michael Faraday reported existence of a dark space in the region of discharge which is now coined after him [45]. The glow discharge is created in the following way: A potential difference V is applied to the electrodes separated by a distance d and the inter electrode space is kept at a constant pressure p, which can result in a breakdown. An additional detail is that the gap distance should be large enough to allow electrons to gain enough energy for ionization of neighboring atoms. The size of the breakdown potential depends on p and d. In 1889, Friedrich Paschen made the first studies on this relation between breakdown voltage, pressure and gas species. He introduced what we call now Paschen Curves. Paschen's Law is expressed by the formula

$$V_B = \frac{APd}{ln(Pd)+B} \quad (3.2)$$

where A and B are constants and V_B is the breakdown potential [48] depending on the species of gas used. Values of coefficients A and B for various gases are given in Table 3.1.

Table 3.1: Values of coefficients A and B for various gases

Gas	**A** (1/cm.mm.Hg)	**B** (V/cm.mm.Hg)
N_2	12	342
H_2	5.4	139
Air	15	365
Ar	12	180
He	3	34

For instance, Paschen's curves for some gases are tabulated and given in Figure 3.2. As it can be seen from the curves, when the product pxd value is very low, few collisions and few secondary electron emissions occur, thus ionization can be only sustained by applying very high potentials. Also, at high values of pd, there exists frequent collisions and electrons cannot gain enough energy to ionize atoms and the discharge is thus attenuated, requiring a high potential value again. Also, the electrodes should be as wide enough so as to prevent the loss of charges through the sidewalls of the inter electrode space.

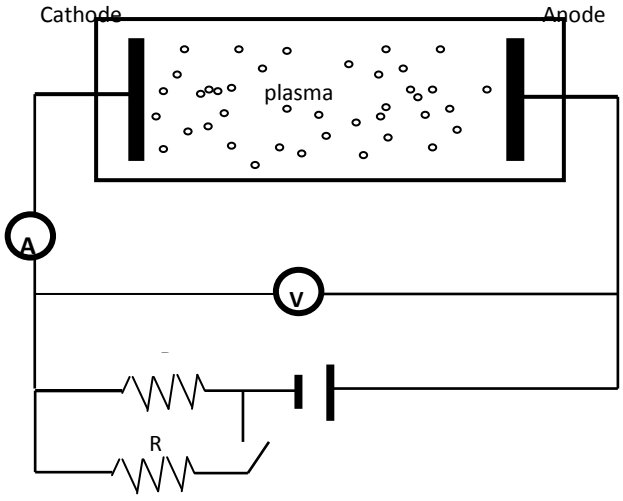

Figure 3.1: DC Discharge experimental Set-up

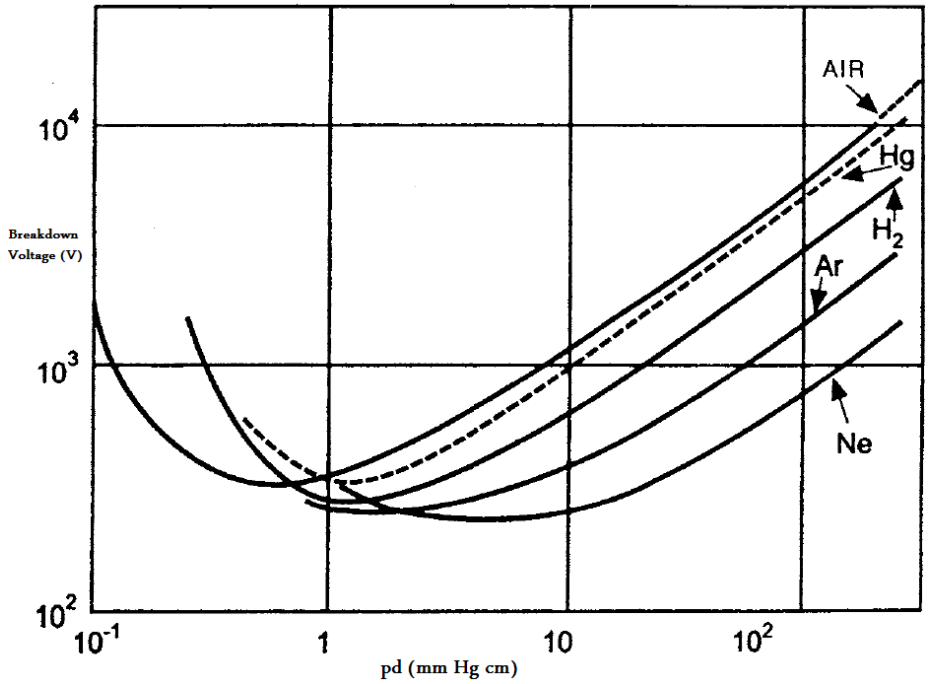

Figure 3.2: Paschen Curve for some gases [48].

As it can be seen from figure 3.2, typical values of breakdown potential are in between 100 V and 10000 V with corresponding pd values in the range 0.1 -100 mm.Hg.cm.

After formation of the plasma, by the spark discharge, there are bands (regions) of glow. Then by adjusting the current, a stabilized current can be established. The glow potential which is the potential drop across the discharge is always less than the minimum breakdown potential shown in figure 3.2. Although the band distribution between the electrodes is determined by the gas type and some other conditions, a typical distribution can be estimated like in the figure 3.3. As it can be seen from the figure above, Aston Dark Space is a thin layer in front of the cathode. Next to it, a Cathode Glow region exists which is also a thin layer. After it, a darker region named Cathode Dark Space stands with both a drop in high potential and electric field. In addition, it is characterized by positive space charge. There is an inverse relationship between gas pressure and the width of it, i.e. if the pressure is decreased, the width of this space increases. Following it, another glow called Negative glow appears. This is the brightest region with the slowest electrons.

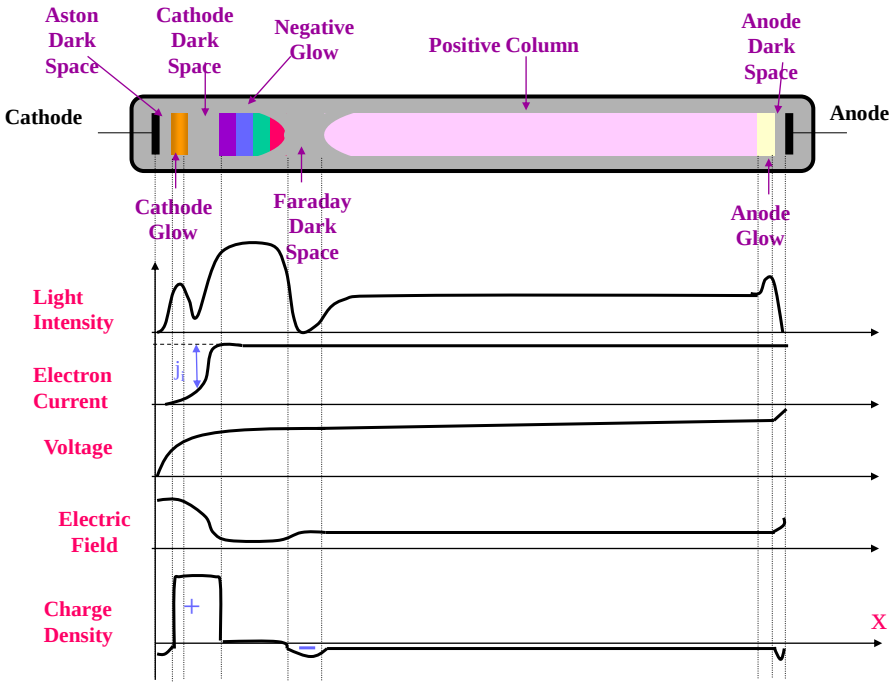

Figure 3.3: Typical distribution of glow [66].

Then, there is an almost completely dark space, a Faraday Dark Space situated afterwards as a transition region. After, there follows another relatively luminous region, called a Positive Column, which is quasineutral, and has a uniform glow, known as the discharge plasma. The electric field through the positive column is also uniform. In the anode side, the brightest region of the glow lies between the Positive Column and the Anode Dark Space which is named Anode Glow. Additionally, when the distance between electrodes is reduced and the current is kept constant, all the regions stated above do not change except for the positive column. It decreases with the decreasing gap (distance between the electrodes) [45]. The color and intensity of the glow depend on the type of gas and the pressure. The intensity of the glow increases with increasing current [45].

According to the voltage-current characteristics of a glow discharge, it can be divided into three main regions; subnormal, normal and abnormal glow discharge [45, 48]. As it can be seen from Figure 3.4, the potential difference of the gap is almost independent from the current, i.e. potential drop in the gap is constant with changing current in the normal region in the figure between the current values 10^{-4}-10^{-2} A.

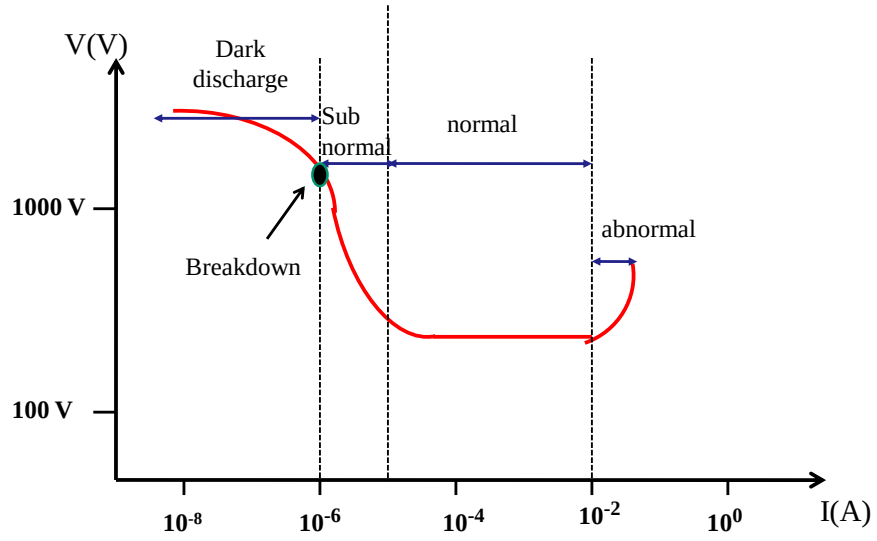

Figure 3.4: V-I Characteristics of Glow Discharge [41].

The potential drop across discharge is little more than the minimum breakdown voltage on Paschen's curve (if the same type of gas and electrodes are used to determine minimum breakdown voltage and discharge potential) [47]. The current at the cathode remains unchanged in the normal glow discharge due to the expansion of the cross-section area of the discharge (parallel to the cathode) proportionally increases as the current increases [48].

From the figure, for lower currents, the potential increases and the sub-normal region begin. On the other hand, if the current is increased, the glow covers the whole cathode surface and a further increase of current is only possible by an increase in the current density. So a larger cathode emission is required which increases the cathode fall in turn. This region is called the abnormal glow.

3.2.1. Excitation and Ionization

First of all, excitation and ionization caused by the) collisions are the most important types of collision in the discharge. The electrodes and the purity of the gas also plays an important role in characterizing the discharge, this will be explained later. The process of transition between the states of an excited particle may cause

photon emission ($\Delta E=h\nu$) (radiative and non-radiative transitions). Thus, the luminous glow is produced by electrons having enough energy to generate light in the visible spectrum by collisions resulting in excitation and de-excitation of the atoms. If the electron in an atom acquires extra sufficient energy to break up the bonding and escape from the atom, the atom becomes positively ionized. Since collision of an electron with sufficient energy with an atom or molecule in a gas causes ionization, electron moving in an electric field can produce more electrons. This process leads to an amplified current in the gas. Soon, electron and ion distribution fill the space between the electrodes. In detail, electrons leaving the cathode pass through the cathode region and then reach to the positive column. Finally, they arrive to the anode. The flow of current through cathode region can be understood by considering the electric field. The field is large at the cathode region and it decreases through the negative glow. After it reaches a minimum it increases again. Electrons are accelerated by the strong electric field but they cannot ionize many particles due to the fact that the electrons do not have enough energy. Then it passes through the weakest electric field region and ionizes more efficiently because it has gained the required energy. In the boundary of negative glow where the field has a minimum, only fast electrons having enough energy are able to still ionize. Even still, the boundary is passed by a very large number of electrons and these contribute into the negative glow. In the cathode region, increase in the number of electrons leads to a large number of ions which form the positive space charge. The positive ions move through to the cathode and finally hit it and they lead to the further secondary electron emission from the cathode.

The electrons entering the negative glow can also be analyzed according to their energy. A few of them have not experienced enough inelastic collision and are fast, and a large number of them which suffered from inelastic collisions are consequently slow. The slow ones have energies lower than the ionization energy but above the excitation energy. Thus, they experience many exciting collisions that contribute to the formation of the negative glow. After electrons get out from the negative glow, they passed to the positive column. Throughout the positive column the electric field is constant and it rises again in the anode region.

The whole ionization mechanism in the gas is divided into two parts: primary and secondary ionization. Primary ionization can be explained by Townsend coefficient [48]. The number of electrons generated between the parallel plate electrodes which are separated with a distance d is given by the formula $N = N_0 e^{\alpha d}$ where N_0 is the initial number of electrons and α (which should be a positive number) is the Townsend coefficient which can be regarded as the average number of electrons produced per electron per cm [45]. When the ionization is initiated, electrons accelerated toward the anode ionize the gas and expand in number according to the above relation. Meanwhile, ions are accelerated toward the cathode by the electric field.

Secondary ionization occurs mainly from ions hitting the cathode. In order to release an electron from a solid, energy of the incident electron should be greater than the work function of the electron. The equation

$$I = I_0 \frac{e^{\alpha d}}{1-\left(\frac{\omega}{\alpha}\right)\{e^{\alpha d}-1\}} \tag{3.3}$$

where ω/α is known as the Secondary Townsend Coefficient. It determines the secondary electron emission from the cathode per incident primary ion. After the ionization is initiated by electrons, more ions reach the cathode and this leads to secondary emission of electrons from cathode [48]. Additionally, the average number of ions produced by an electron per volt of potential difference can be given by $\eta = {\alpha d}/{V}$ or 1/η, one volt per ionization, both are important parameters for understanding the discharge [48]. In a glow discharge, it has been proven that the current is carried by electrons, nevertheless, near the electrodes either electrons or ions are dominant [45]. Therefore, they should be considered individually in these regions.

3.2.2. Anode

Electrons are generally the current carriers near the anode for most commonly used electrode materials. The slow electrons supplied from the positive column are attracted by the anode and likewise positive ions are repelled by it. Hence, negative space charge is formed near anode leading to an increase in the electric field and

potential. As a result, potential drop is observed that is named the anode fall which is referring to the Anode Dark Space. Electrons coming from the positive column enter the anode fall region with a small initial energy and then they are accelerated towards the anode. Following the anode dark space, they have acquired enough energy to excite or ionize atoms. Thus, anode glow is formed.

3.2.3. Cathode

As the nature of the electrodes and gases determines the primary and secondary ionization coefficients, the value of the potential in the cathode region is significantly affected by the impurities in the gas and clearness of the cathode (particles on the cathode surface ruin the purity of the gas inturn. Also, the work function of the material is very important. If the value of the work function is low, the secondary emission is high. It's observed that the positive space charge region separated from the cathode by Cathode and Aston Dark spaces is plane parallel to the cathode. The potential drop across these dark layers is named as the Cathode Fall. Generally, the value of the cathode fall potential is identical to the minimum breakdown potential [45]. The value of the cathode fall is higher than the value of the anode fall due to the greater space charge effects. Space charges distributed near the cathode and anode regions (positive space charge at cathode region and negative space charge at anode region) would produce field distributions in that regions. Since space charge of the slower ions in the cathode region is more than the fast electrons in the anode region, the amount of decrese in the potential is larger in the cathode region [45]. In fact, most of the potential drop exists between the cathode and the negative glow. And most of the power is dissipated in this region. Cathode fall potential can be found by the formula [47],

$$V_{cn} = \frac{1}{\eta} ln\left(1 + \frac{1}{\omega/\alpha}\right) \tag{3.4}$$

where η is the the average number of ions produced by an electron per volt of potential difference and ω/α is the Secondary Townsend Coefficient. It is clear from this formula that the cathode fall potential increases with decreasing secondary electron emission. Also, it strongly depends on the purity of the gas and the cathode

material. V_{cn} is larger in molecular gases compared to rare (elemental gases) ones for a given cathode material [48].

3.3. Electromagnetic waves in Plasma

To understand the dielectric properties of the plasma, we used the Drude model, since it describes the behavior of an electron gas. The equation of motion for a free electron is given by:

$$m\left[\frac{d^2x(t)}{dt^2} + \gamma_p \frac{dx(t)}{dt}\right] = -eE(t) \tag{3.1}$$

where γ_p is the collision per second and magnetic field effects (as well as resonance conditions) are ignored [59]. If the electric field is of the form $E(t)= E_0(\omega)e^{i\omega t}$ then the solution of the differential equation for x(t) gives us the form of $x(t)=X_0(\omega)\ e^{i\omega t}$ where E_0 and X_0 are the complex amplitudes. Inserting x(t) into the equation we find

$$X_0(\omega)= eE_0(\omega)/m(\omega^2-i\gamma_p\omega) \tag{3.2}$$

In addition, electric polarization (the dipole moment per unit volume) is $P(\omega)=-en_eX_0(\omega)$ and then inserting X_0 gives

$$P(\omega)= -e^2n_eE_0(\omega)/m(\omega^2-i\gamma_p\omega) \tag{3.3}$$

where n_e is the electron density. We also know that $P(\omega)=\varepsilon_0\chi E_0(\omega)$ where χ is the electric susceptibility. Equating P(ω)'s, we arrive at an equation for

$$\chi= -e^2n_e/m\varepsilon_0(\omega^2-i\gamma_p\omega) \tag{3.4}$$

Next, knowing plasma frequency $\omega_p = \left(\frac{n_e e^2}{\varepsilon_0 m_e}\right)^{1/2}$, we can rewrite as

$$\chi=- \omega_p^2/ \omega^2-i\gamma_p\omega \tag{3.5}$$

Then, using dielectric function relationship $\varepsilon/\varepsilon_0= 1+ \chi$, we arrive at

$$\frac{\varepsilon(\omega)}{\varepsilon_0} = 1 - \frac{\omega_p^2}{\omega^2 - i\omega\gamma_p} \tag{3.6}$$

Following this, we will use $n(\omega) = \sqrt{\frac{\varepsilon(\omega)}{\varepsilon_0}} = \eta - i\kappa$ to find the real and imaginary parts of the complex refractive index

$$\frac{\varepsilon(\omega)}{\varepsilon_0} = 1 - \frac{\omega_p^2}{\omega^2 - i\omega\gamma_p} = n^2 = (\eta - i\kappa)^2 \tag{3.7}$$

Multiplying the complex term on the right hand side with its conjugate $\frac{1}{\omega^2 + i\omega\gamma_p}$, we will get

$$1 - \left[\frac{\omega_p^2}{\omega^2 + \gamma_p^2} + i\left(\frac{\omega_p^2}{\omega^2 + \gamma_p^2}\right)\frac{\gamma_p}{\omega}\right] = (\eta - i\kappa)^2 \tag{3.8}$$

To solve the equation, let's call $u = \frac{\omega_p^2}{\omega^2 + \gamma_p^2}$ and $v = \frac{\gamma_p}{\omega}$, therefore the equation is simplified to $(1 - u - iuv) = (\eta^2 - \kappa^2 + i2\eta\kappa)$. By equating complex and imaginary parts each other, we get $\eta^2 - \kappa^2 = 1 - u$ and $-uv = 2\eta\kappa$ where $\kappa = \frac{-uv}{2\eta}$. Inserting κ in the first equation, one will find $\eta^2 - \frac{u^2v^2}{4\eta^2} = 1 - u$ which leads to $4\eta^4 - u^2v^2 = 4\eta^2 - 4\eta^2 u$. Replacing the terms in the previous equation results in the equation $4\eta^4 + \eta^2(4u - 4) - u^2v^2 = 0$ and solving the equation to find η gives

$$\eta_{1,2}^2 = \frac{(4-4u) \pm \sqrt{(4u-4)^2 + 16u^2v^2}}{8} \tag{3.10}$$

Further simplification gives $\eta_{1,2}^2 = \frac{1-u \pm \sqrt{(u-1)^2 + u^2v^2}}{2}$. Finally, what we have is

$$\eta_{1,2} = \pm\left(\frac{1-u \pm \sqrt{(u-1)^2 + u^2v^2}}{2}\right)^{1/2} \tag{3.11}$$

To decide which root is the solution we look for, we consider that η should be real and positive to get:

$$\eta = \left(\frac{1-u + \sqrt{(u-1)^2 + u^2v^2}}{2}\right)^{1/2} \tag{3.12}$$

Then, keeping on our work to find imaginary part provide us the equation as follows:

$$\kappa^2 = \eta^2 - 1 + u = \frac{1-u+\sqrt{(u-1)^2+u^2v^2}}{2} + u - 1 = \frac{-1+u+\sqrt{(u-1)^2+u^2v^2}}{2} \quad (3.13)$$

which gives the result as

$$\kappa_{1,2} = \pm\left(\frac{-1+u+\sqrt{(u-1)^2+u^2v^2}}{2}\right)^{1/2} \quad (3.14)$$

κ should be real and positive to guarantee attenuation, so

$$\kappa = \left(\frac{-1+u+\sqrt{(u-1)^2+u^2v^2}}{2}\right)^{1/2} \quad (3.15)$$

Eventually, inserting u and v into the equations, we will get

$$\eta = \left\{\frac{1}{2}\left(1 - \frac{\omega_p^2}{\omega^2+\gamma_p^2}\right) + \frac{1}{2}\left[\left(1 - \frac{\omega_p^2}{\omega^2+\gamma_p^2}\right)^2 + \left(\frac{\omega_p^2}{\omega^2+\gamma_p^2}\frac{\gamma_p}{\omega}\right)^2\right]^{1/2}\right\} \quad (3.16)$$

$$\kappa = \left\{-\frac{1}{2}\left(1 - \frac{\omega_p^2}{\omega^2+\gamma_p^2}\right) + \frac{1}{2}\left[\left(1 - \frac{\omega_p^2}{\omega^2+\gamma_p^2}\right)^2 + \left(\frac{\omega_p^2}{\omega^2+\gamma_p^2}\frac{\gamma_p}{\omega}\right)^2\right]^{1/2}\right\} \quad (3.17)$$

The simulations of real and imaginary parts of the refractive index for some electron densities is given in figure 3.5 and 3.6.

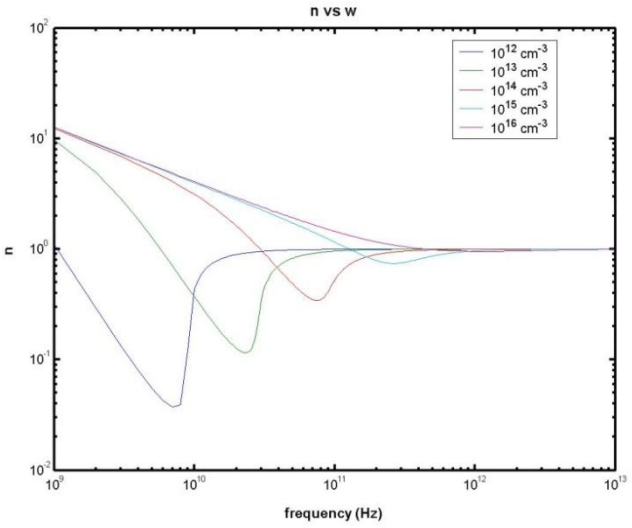

Figure 3.5: Real part of refractive index for various electron densities

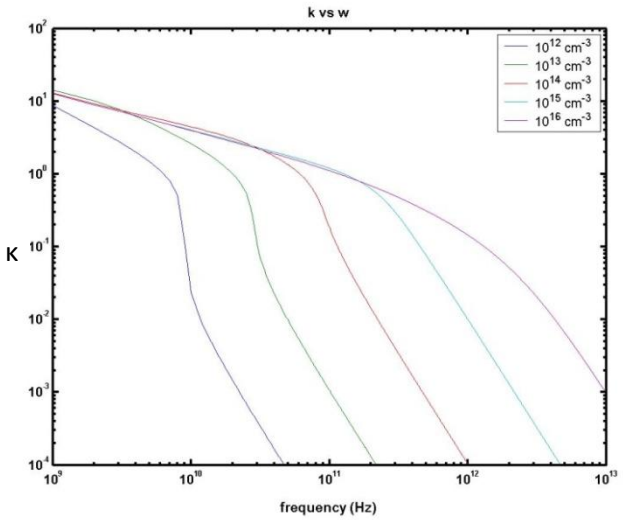

Figure 3.6: Imaginary part of refractive index for various electron densities

By using the real and imaginary parts of the refractive index, we derive the formula of conductivity as follows;

$$\sigma = \frac{\omega\eta\kappa}{2\pi} + i\frac{\omega}{4\pi}[1 - (\eta^2 - \kappa^2)] \tag{3.18}$$

Then, ploting real and imaginary conductivity yields the graphs in figure 3.7 and 3.8.

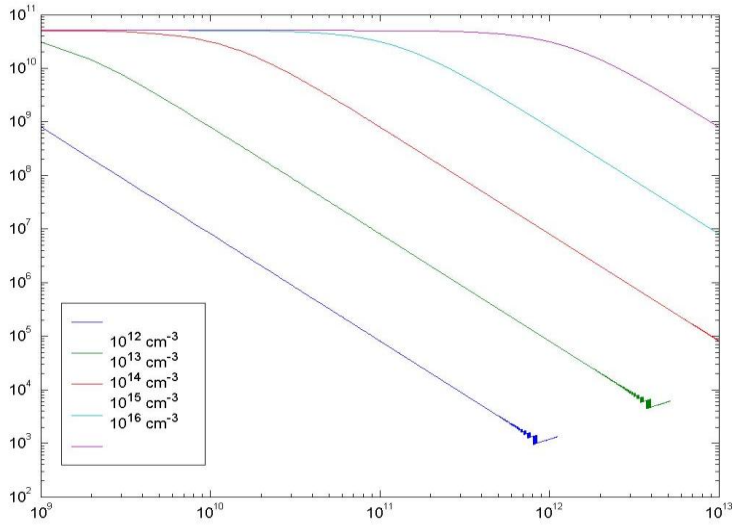

Figure 3.7: Real part of the conductivity

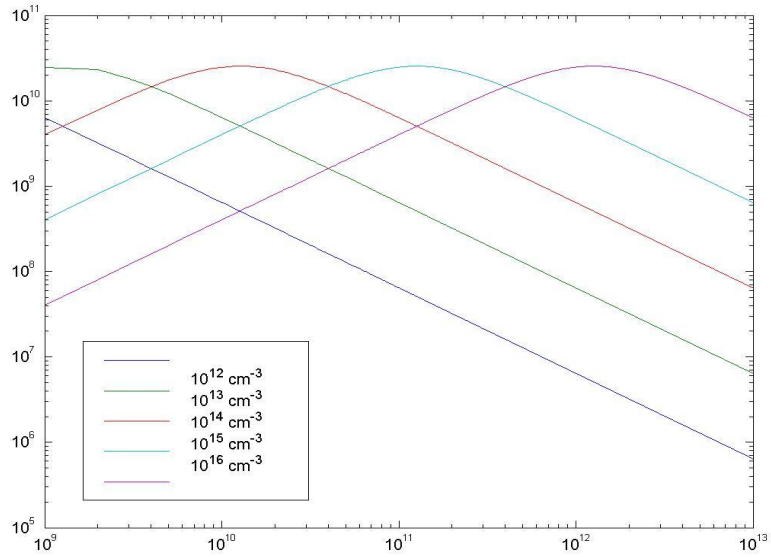

Figure 3.8: Imaginary part of the conductivity

Now, we can consider the transmission behavior of electromagnetic waves from plasma by using Fresnel coefficients for one layer.

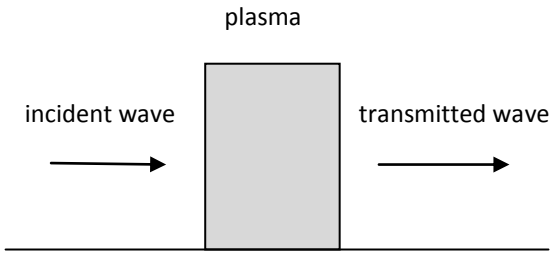

Figure 3.9: Illustration of one layer plasma

General transmission relations for one layer medium are given as

$$t = \frac{t_{12}t_{21}e^{-i\varphi}}{1-r_{21}r_{23}e^{-i2\varphi}} \tag{3.18}$$

with $t_{12} = \frac{2n_1\cos\theta_1}{n_1\cos\theta_2+n_2\cos\theta_1}$. Using $t_{12}t_{21} - r_{12}r_{21} = 1$, $r_{21} = -r_{12}$ and $\varphi = \frac{2\pi\kappa d}{\lambda}$ with d=0.1 m we will have $t_{12}t_{21} = 1 + r_{12}r_{21} = 1 - r_{12}^2$ which gives the relation $r_{12}^2 = 1 - t_{12}t_{21}$, thus we get

$$t = \frac{t_{12}t_{21}e^{-i\varphi}}{1-(1-t_{12}t_{21})e^{-i2\varphi}} \tag{3.19}$$

Then we can find transmission as

$$T = tt^* = \frac{(t_{12}t_{21})^2}{1+(1-t_{12}t_{21})^2-(1-t_{12}t_{21})e^{-i2\varphi}-(1-t_{12}t_{21})e^{+i2\varphi}} \tag{3.20}$$

Using $e^{\pm i\theta} = \cos\theta \pm i\sin\theta$ to find

$$T = \frac{(t_{12}t_{21})^2}{1+(1-t_{12}t_{21})^2-(1-t_{12}t_{21})(\cos 2\varphi - i\sin 2\varphi + \cos 2\varphi + i\sin 2\varphi)} \tag{3.21}$$

Then, we will get

$$T = \frac{(t_{12}t_{21})^2}{1+(1-t_{12}t_{21})^2-(1-t_{12}t_{21})\,2\cos 2\varphi} \tag{3.22}$$

By inserting $t_{12} = \frac{2}{1+n}$, $t_{21} = \frac{2n}{1+n}$, $t_{12}t_{21} = \frac{4n}{(n+1)^2}$ and $(t_{12}t_{21})^2 = \frac{16n^2}{(n+1)^4}$ we find the relation as follows for normal incidence:

$$T = \frac{16n^2}{(n+1)^4+(n-1)^4-(n^2-1)^2 2cos2\varphi} \tag{3.23}$$

The figures below show the wave transmissions from plasma for various electron densities.

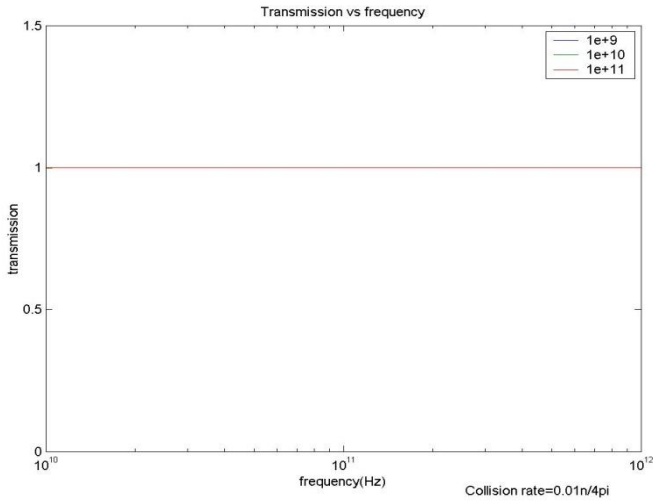

Figure 3.10: Transmission between 0.01 THz and 1 THz for electron densities 10^9 to 10^{11}.

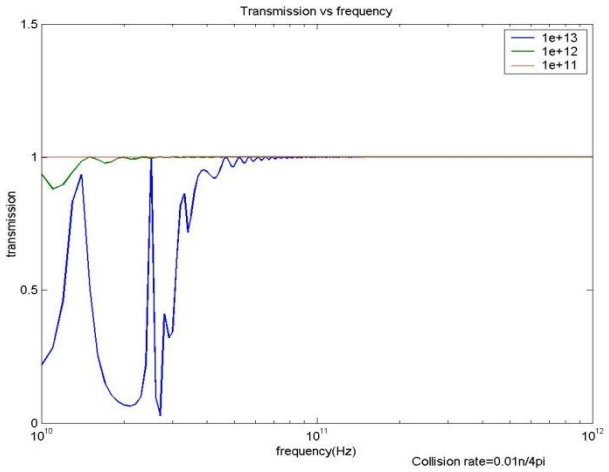

Figure 3.11: Transmission between 0.01 THz and 1 THz for electron densities 10^{11} to 10^{13}.

As it can be seen from figures, transmissions are unity for low electron densities whereas it approaches to unity for high electron densities. Therefore, we can conclude that according to Drude Model, for low electron density plasmas i.e. cold plasmas, transmission of electromagnetic waves through it are not affected by the plasma.

In the next chapter, we will continue with the experimental instrumentation. The specifications of the instruments and the schematic representations of the set up will be given. The following chapter contains experimental data and results of the experiment.

CHAPTER 4

DESCRIPTION OF EXPERIMENTS

In this section, a detailed explanation of the experimental set up will be given. The set up is made up of three parts, the THz TDS System, the Vacuum System and the Emission Spectrometer. These techniques are applied towards characterizing a DC glow discharge plasma.

4.1 THz TDS System

An ultrafast laser beam is a requirement for coherent THz pulse generation and detection. In our system a mode-locked Ti-Sapphire laser was employed with a central wavelength of approximately 800 nm which corresponds to an energy of 1.55 eV per photon. Each pulse had a duration of 15 fs and the repetition rate was 75 MHz. The average power of the laser was around 300 mW.

In the THz-TDS system (see figure 4.1) the visible laser beam is split into a THz generation and THz detection arm. By using a 50:50 beam splitter, each pulse that arrives is split into two. In the generation arm the average laser power was nearly 60 mW whereas in the detection arm it was around kept around 15 mW with the aid of a neutral density filter. In order to measure the THz pulse (see chapter 2) optical path lengths both in generation and detection arms should be identical. Careful attention must be given to ensure the same height is kept for the beam through the whole system and it should be aligned in straight paths. Following the beam splitter in the generation arm, we used a Newport M 20X objective (Plan Achromat) with a numerical aperture 0.40 in order to focus the beam on the generation antenna.

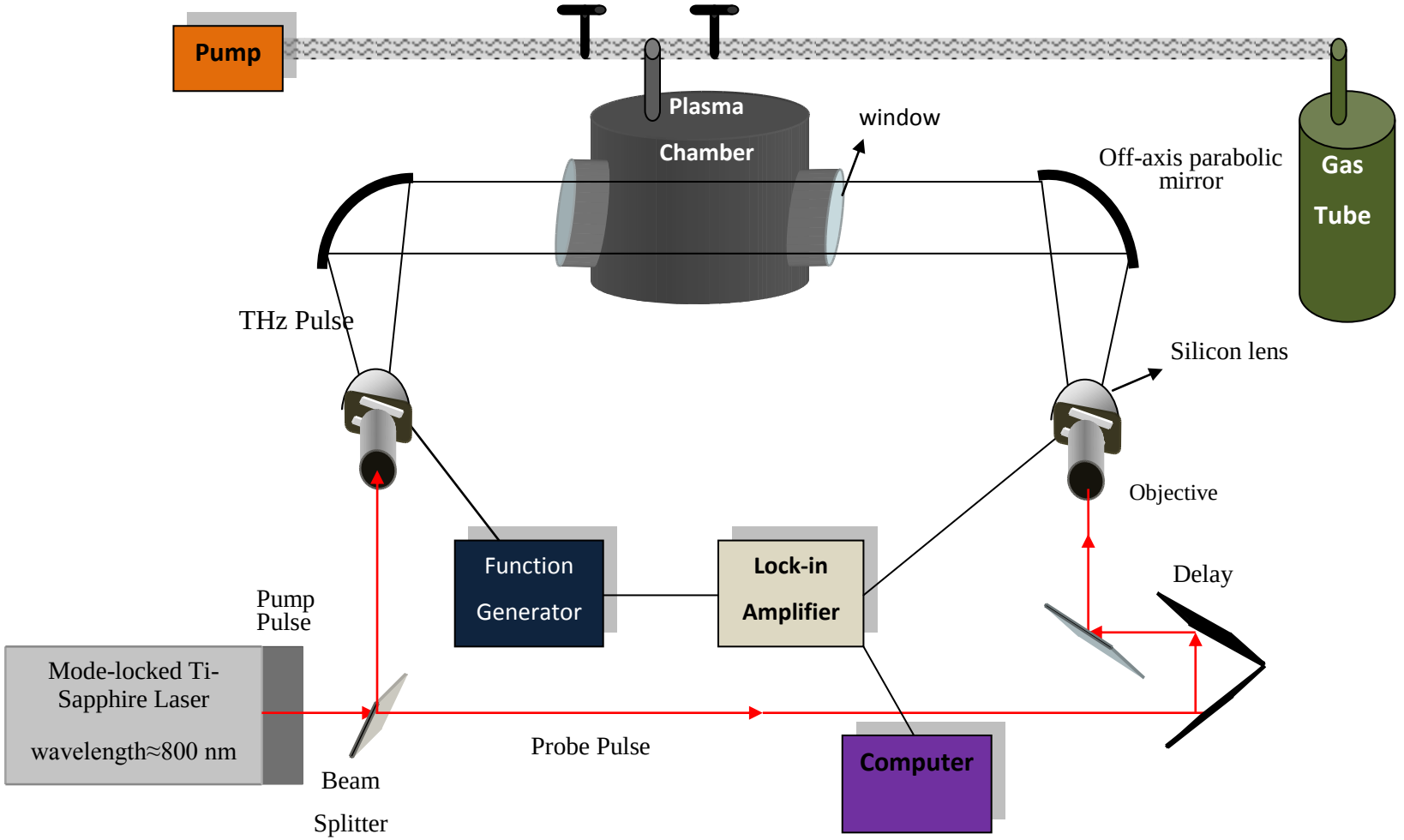

Figure 4.1: THz-TDS System for plasma diagnostics

The dipole gap of the antenna (see chapter 2) was placed on the focus of the objective to obtain a large gain in the THz signal. In order to determine the antenna position accurately, it was placed on a xyz translational stage which enables us to move the antenna in three dimensions. The antenna position was determined by connecting it to an ohmmeter and finding the minimum resistance, which in turn occurs at the dipole gap.

The generation antenna used in this system was BATOP PCA-44-06-10-800-x with laser excitation wavelength 800 nm, length 44 μm, dipole gap 6 μm and width 10 μm [62]. Furthermore, optical properties and electrical properties can be seen in Table 4.1 and 4.2 respectively. Also, schematic diagram and images of it is given in Figure 4.2. The dark resistance of this antenna was about 25 MΩ and it was about 300 kΩ after the visible laser beam was focused onto the gap.

The dynamics of THz generation were explained in chapter 2, and it depends on the photon energy and the band gap of the antenna substrate, in this case, LTG-GaAs. LTG-GaAs is a direct band gap semiconductor with a band gap similar top GaAs, about 1.43 eV. Decay time of the electron is about 100 ps in GaAs and on the order of 400fs in LTG-GaAs. After our laser pulse with average photon energy of 1.55 eV is absorbed in the substrate it gives rise to a transient current in the antenna due to a voltage bias on the gap. Bias voltage should be applied to the antenna to accelerate created carriers, and when using phase sensitive detection techniques a function generator is needed to modulate the phase and thus the bias.

Table 4.1: Electrical Properties of the PCA-44-06-10-800-x [62].

Electrical Parameters	**Minimum Ratings**	**Standard**	**Maximum Ratings**
Dark Resistance	20 MΩ	25 MΩ	30 MΩ
Dark Current at 10V	300 nA	400 nA	500 nA
Voltage		20 V	50 V

Table 4.2: Optical excitation parameters of PCA-44-06-10-800-x [62].

Optical Excitation Parameters	Minimum Ratings	Standard	Maximum Ratings
Excitation laser wavelength	500 nm	800 nm	850 nm
Optical reflectance at 1040 nm	7 % at 500 nm	5 % at 800 nm	7 % at 850 nm
Optical mean power	-	30 mW	80 mW
Optical mean power density	-	100 kW/cm^2	200 kW/cm^2
Carrier recovery time	-	400 fs	-

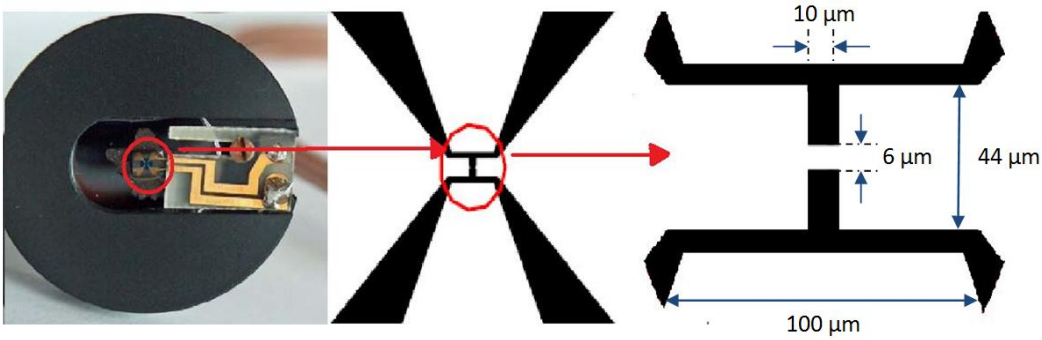

Figure 4.2: Photo and schematic diagram of the PCA-44-06-10-800-x [62].

A HP 3310A function generator was used in our experiment. A +/- 15 V potential difference was applied to the PC antenna and the frequency of the function generator was kept at 2500 Hz. The function generator was connected to the lock-in amplifier to provide the reference phase information necessary for detection. Attached to the back side of the antenna, was a hemispherical silicon lens to reduce the divergence of the beam at the air substrate interface. Next, the generated THz

was collimated by using a 90 degree off-axis parabolic mirror with a diameter of 50 mm and focal length of about 80 mm. Hence, the reflected THz beam from the mirror would become circular with a beam diameter of 50 mm. The beam traveled through a distance of roughly 60cm before being detected after a second 90 degree off-axis parabolic mirror. In between the parabolic mirrors we placed a specially designed plasma chamber. The collimated THz beam passes through the plasma chamber through two view ports. These view ports have a 62mm diameter and are made of a glass that can withstand the low pressure in the chamber, namely Kodiac glass. Kodiac glass is a type of glass which has lead in it. After passing though the chamber the THz pulse was focused on to the hemispherical silicon lens on the detection antenna by using another identical 90 degree off-axis parabolic mirror.

In the detection arm, following the beam splitter, the laser pulse was first sent through an attenuation filter to lower the power, and then aligned off a corner cube which was mounted on a mechanical translational stage used to change the delay between generation and detection arms (THz pulse at the detector and visible detection pulse at the detector). After the corner cube, the beam was directed to an objective which was located just before the detection antenna. The objective used here was an Olympus Plan N 40X with a numerical aperture of 0.65. There was no bias applied to the detection antenna. As explained in chapter 2, the THz electric field acts like a bias leading to the movement of carriers across the detection antenna dipole gap. As there is no electric field after the THz passes, the carriers cannot get back as they are trapped. Rather than this, the charge flows into the lock-in proportional to the THz electric field. The detection antenna used in this system was BATOP PCA-40-05-10-800-xwith laser excitation wavelength 800 nm, length 44 μm, dipole gap 6 μm and width 10 μm [63]. Schematic diagram of it is given in Figure 4.3. Furthermore, optical properties and electrical properties can be seen in Table 4.3 and 4.4 respectively.

The dark resistance of this antenna was about 3 MΩ and it was about 180 kΩ when the visible pulse was focused onto the gap. The substrate material of the detection antenna was LTG-GaAs. Band gap of the LT- GaAs is same with regular GaAs, however, decay time of carriers is 0.4 ps. In order to detect 2 THz using PC

antenna, carriers decay time must be smaller than 500 fs (1/2THz= 500 fs), so LTG-GaAs is used.

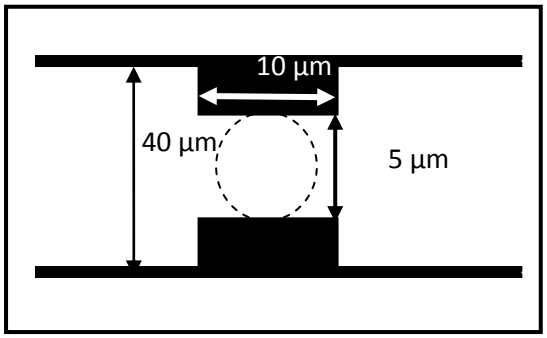

Figure 4.3: Schematic diagram of PCA-40-05-10-800-x [63]

The current is measured with the lock-in amplifier, Stanford research Systems SR530. By changing the delay between the THz pulse and detection pulse we obtain the whole THz waveform. Lock-in amplifier is the key element in our experiment as it allows us to obtain both phase and the magnitude of the measured signal i.e. measured signal is proportional to the THz electric field. The reference signal for the lock-in amplifier was given by the function generator. Thus, input signals that have frequencies different from the reference signal give near zero as an output (after we adjust the phase of the lock-in). The current sensitivity of SR530 is 100 fA to 0.5 µA [53], depending on the connections used between the antenna and the lock-in. Computer controlled data acquisition was done for this experiment by employing LabView software.

Table 4.3: Electrical Properties of the PCA-40-05-10-800-x [63].

Electrical Parameters	**Minimum Ratings**	**Standard**	**Maximum Ratings**
Dark Resistance	2 MΩ	2.5 MΩ	3 MΩ
Dark Current at 10V	3 µA	4 µA	5 µA
Voltage		20 V	30 V

Table 4.4: Optical excitation parameters of PCA-40-05-10-800-x [63].

Optical Excitation Parameters	Minimum Ratings	Standard	Maximum Ratings
Excitation laser wavelength	500 nm	800 nm	850 nm
Optical reflectance at 1040 nm	7 % at 500 nm	5 % at 800 nm	7 % at 850 nm
Optical mean power	-	30 mW	80 mW
Optical mean power density	-	100 kW/cm^2	200 kW/cm^2
Carrier recovery time	-	400 fs	-

The delay was changed by the help of a Thorlabs APT controller which was controlled by the LabView program. In the LabView program we were able to see both time domain and Fourier Transformed frequency domain data simultaneously. In order to apply the Fast Fourier Transform algorithm, number of data points in the waveform needs to be 2^n. After the data was taken, we used Origin plotting software to analyze and graph our results.

The resolution of our waveform in the frequency domain measured in terahertz depends on the time length of the time domain waveform measured in picoseconds which in turn is controlled by the mechanical stage where the corresponding length for 1ps = 300μm in air. The scanning length for our system was a maximum of 50 mm. The scanning interval was determined by the position of THz (where the peak was in this 50mmm scan window), the step size in microns which corresponds to the maximum observable frequency after the Fourier transform and the number of data points required for a Fast Fourier Transform (either 512, 1024 or

2096). The start and finish positions, the step size and the wait time duration between each measurement/step are arranged through our LabView program. The step size was typically taken as 20 μm which corresponds to 40microns on the step size of the mechanical stage due to the round-trip off the corner cube, which in turn corresponds to roughly 8THz of bandwidth - more than enough for our detection system which has a maximum bandwidth of 2.5THz due to the relaxation time of carriers in the detection antenna. The wait time between each step (data point) was typically 600 ms for our system, where the wait time was taken to be twice the averaging time per data point of the lock-in amplifier which was typically 300ms - typically a wait time of 3 times the averaging time is taken in electrical measurement systems (1/e rule).

The main advantage of THz spectroscopy is that it allows us to measure the electric field instead of measuring the intensity of the THz pulse. Therefore, we have obtained data about the amplitude change and the phase change of the electric field as the pulse passes through the plasma. As a result, we can obtain the complex index of refraction. A photograph of the experimental set up is given in Figure 4.2.

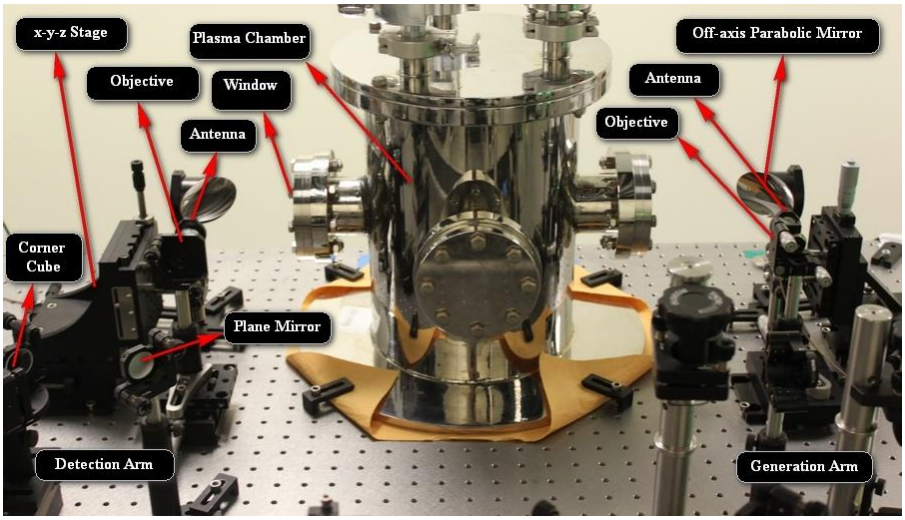

Figure 4.4: Photograph of the set up in the laboratory. The plasma chamber was built using the industrial manufacturing capabilities of the industry in Ankara, Turkey. The plasma chamber consists of two 12cm diameter steel electrodes with ad adjustable gap distance which was generally kept larger than the THz beam path of 50mm (This distance was actually kept closer to 9cm to probe the positive and negative regions of the plasma effectively)

4.2 Vacuum and DC Bias System

The vacuum system we used in this work mainly consists of 3 parts: the mechanical rotary pump, the turbo-molecular pump and the plasma chamber. The system configuration is given in figure 4.6.

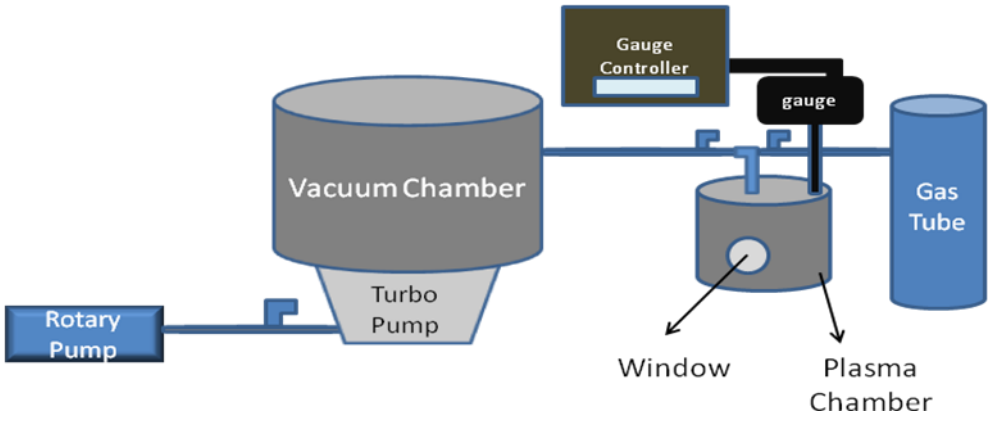

Figure 4.5: Vacuum System

The first element in the figure is a rotary pump. A Varian DS 302 rotary pump was used to initially pump down our plasma chamber to a pressure of 10^{-2} Torr. We measured the pressure of the gas by employing a gauge connected to the plasma chamber and a gauge controller allows us to record pressure which is directly connected to the gauge. While doing air plasma experiments we connected the rotary pump directly to the plasma chamber because it was enough to evacuate down to 10^{-2} Torr and generate a plasma in air. On the other hand, while doing gas plasma experiments, we need to evacuate further to guarantee the purity of the gas inside the plasma. Therefore, we used a Turbo Molecular Pump TV 551 Navigator to pump down to 10^{-4} Torr. Unfortunately we could not pump the plasma chamber directly due to the fact that the turbo molecular pump could not connect directly to our chamber. That is why we used an intermediary chamber between the turbo pump and the plasma chamber, thus our lowest pressure was 10^{-4} Torr. In order to operate turbo pump, the pressure of the system had to decrease to at least 10^{-2} Torr. Only after then, was the turbo pump turned on.

The plasma chamber was a steel cylindrical chamber having two windows in order to enable transmission of THz pulses. The height of the windows is determined by considering the height of the THz pulses on the optical table which means that we had to consider the diameter and height of the off-axis parabolic mirrors. Kodiac glass was selected to allow pumping down to low pressures. The disadvantage of using kodiac is that approximately two third of the THz power is absorbed by it (this is due to the fact that Kodiac glass has metal particles which in turn scatter and reduce the THz transmission – as will be seen in chapter 5, this was also the reason why the bandwidth of the THz pulse did not go beyond 0.4THz). The electrical connection was set from the side of the plasma chamber, and the vacuum system connections were done through the upper part of the plasma chamber. Planar electrodes with a diameter of 12 cm were located inside upper and lower part of the chamber. The separation between them was 88mm. They were connected to a high voltage power supply. The power supply we have used was prepared by one of the researcher at our department which rectifies AC to DC allowing us to apply potentials as high as 3000 V.

By applying a DC bias to the electrodes, the plasma is formed in the inter electrode space. The plasma can be generated for different discharge currents, and different pressures but we wanted to concentrate on regions when the plasma vas visibly stable – i.e. not fluctuating. This limited the range of discharge currents and pressures we could investigate the plasma confidently. Applied potential values and corresponding plasma potentials for different pressure and current values for air, gaseous Nitrogen and Argon plasma is given in Figure 4.6.

In addition as was discussed in chapter 3, the low temperature glow discharge plasma has two regions of particular interest: the uniform quasi-neutral region, the positive column and the negative region, the negative glow and dark space. When the upper electrode is connected to the lower voltage terminal and the lower electrode is connected to the higher voltage terminal of the supply, we were able to investigate the anode region of the generated DC discharge plasma between the electrodes or mostly the region containing the positive column. On the other hand, when the upper electrode is connected to the higher voltage terminal and the lower electrode is

connected to the lower voltage terminal of the supply, we were able to investigate the cathode region of the generated DC discharge plasma.

Table 4.5: Applied potential and plasma potential data for changing current and pressure values for different plasma types.

Plasma	Current(mA)	Pressure(Torr)	V_{app} (V)	V_{plasma} (V)
Air	**5**	0.1	400-500	200-250
		0.3	400-500	210-230
		0.5	500	210-230
	10	0.1	900-1000	250-300
		0.3	900-1000	210-250
		0.5	900-1000	210-250
	15	0.1	1400-1600	250-300
		0.3	1400-1500	220-240
		0.5	1400	210-220
N_2	**5**	0.1	400-500	180-210
		0.3	400-500	210-250
		0.5	500	210-230
	10	0.1	900-1000	230-240
		0.3	900-1000	220-240
		0.5	900-1000	200-210
	15	0.1	1300-1500	220-240
		0.3	1400-1500	210-240
		0.5	1400-1500	200-210
Ar	**5**	0.1	300	100-150
		0.3	400	100-150
		0.5	400	100-150
	10	0.1	800	150-200
		0.3	800	150-200
		0.5	800	150
	15	0.1	1300	200
		0.3	1300	150-200
		0.5	1300	150-200

The experiments were done at a pressure in between 0.1-0.5 Torr and discharge currents in the range 5-15 mA. The pressure in the chamber was controlled by valves in 0.1 torr increments and the current was controlled by the applied DC bias in 5mA increments. Electrical connections of the system can be seen in figure 4.6. The current was measured by using an ammeter connected before one of the electrodes and the potential was measured by connecting a voltmeter across the electrodes. The breakdown of the gas between the electrodes is initiated by applying potential when the switch placed before one of the resistors is in the open position. After, the switch is closed, the power on the plasma increases. Thus, a stable glow discharge is formed.

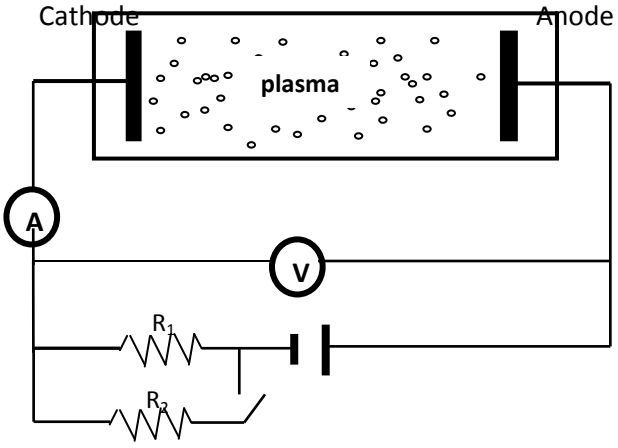

Figure 4.6: Electrical connections of the set up. The typical values of measured potentials by the voltmeter and measured current by ammeter are given in Table 4.5. The resistance of the R_1 is approximately 189 kΩ and R_2 is approximately 186 kΩ.

During measurements of air plasmas we needed a reference scan (as discussed in chapter 2) for the THz- TDS measurements. This reference scan was done with no plasma, at the most minimum value of the vacuum in the plasma chamber. For the air measurements pumping down to 10^{-2} Torr was sufficient. Then the vacuum data was taken before the plasma was created between 0.1 to 0.5 Torr. To adjust the pressure between 0.1 and 0.5 Torr, air is put into the chamber by opening the valve positioned on the chamber. The pressure is set to the intended value and the plasma is generated by applying potential difference to electrodes. To finish the experiment one more vacuum data is taken after the plasma is removed to

observe if a variation occurred in the THz waveform (this can be due to vibrations, laser noise power stability, etc.).

For gas measurements, as already mentioned in the previous part, in order to initiate a gas discharge the plasma chamber should be evacuated to 10^{-4} Torr in order to preserve gas purity. Following this, the vacuum data was taken at this pressure. Then, the gas is injected from the top of the plasma chamber by opening the valve between the chamber and gas tube and the pressure is adjusted between 0.1 and 0.5 torr to the intended value by using the valve between the pump and chamber. The experiments were done by using Nitrogen gas (N_2) and Argon (Ar) gas. The purity of both of them was nearly 99.998 %. Finally, the experiment was completed by taking the vacuum data again to measure any changes in the THz waveform during the measurement.

4.3 Emission Spectroscopy

In addition to the THz-TDS scans we performed measurements of the spectral intensity of the plasma created for different gases (air, nitrogen, argon) at different pressures and discharge currents. Since air is predominantly nitrogen and a small part argon we hoped to see similarities in the measurements. The emission spectra due to the exciting collisions of the dc discharge provide certain information about the active species in plasma. The method is dependent on the fact that intensity of the peak at a certain wavelength generated from an excited state will supply information about the density of species located at that state [56]. As obtaining the spectrum of plasma does not require interaction with it, emission spectroscopy is advantageous since the plasma is not disturbed. The experimental procedure is also simple: the peaks in the spectrum are analyzed and they are matched to their corresponding transition for each species in the plasma. The peak intensities [57] and width of the peak [58] are determined by the discharge conditions in the plasma and can be measured with compact spectrometers. An Ocean Optics HR-2000 spectrometer was employed in our experiments. The range of this detector is between 200 nm to 1100 nm i.e. enabling us to observe intensities of the light between the wavelength 200 nm to 1100 nm. The spectrometer was positioned in front of the window in the detection side and it is adjusted not to block the THz pulse reflected

from the parabolic mirrors during the THz measurements. Then, the spectrum was investigated in terms of the peaks at specific wavelengths and their intensities.

CHAPTER 5

EXPERIMENTAL RESULTS

Up to now, theoretical background and experimental details have been given. Here, we keep on with the results of the experiments we had done. First, we start with the transmission spectrum of the THZ pulse from anode and cathode region of the atmospheric plasma. Then, we will continue with the emission spectrum of air, gaseous Nitrogen and Argon plasma. At the final part, transmission spectrum of gaseous Nitrogen and Argon plasma will be given.

Plasma diagnostics by using THz spectroscopy is a non-contact method compared to other diagnostics tools such as Langmuir Probe which requires inserting probes into the plasma. Here we focus on using THz-TDS techniques to investigate the DC glow discharge plasma. The typical electron density of laboratory plasmas is in the range between 10^8- 10^{14} cm^{-3} corresponding to plasma frequency in the range 90 MHz- 90 GHz [54]. Since DC generated plasmas have very low electron densities, our theoretical simulations shows that the THz transmission through the plasma should not be affected by plasma oscillations according to Drude Theory. This is under the assumption that the collision frequency is taken as $1/100^{th}$ of the plasma frequency [19]. However, our observations show that transmission is affected by the plasma and moreover we find that the THz transmission through the plasma depends on the polarization of the THz electric field i.e. the THz electric field parallel or perpendicular to the applied DC electric field. In addition when we repeat these measurements for different gases, we also find that the type of gas and the pressure of the discharge also play a role in the transmission of the THz radiation.

While the type of gas and the discharge pressure can be important parameters which can be extrapolated to affect the Drude theory (i.e. pressure affects the collision frequency parameter, and the type of gas plays a role in the both the plasma frequency and collision frequency parameters), the model does not account for the polarization of input field, nor does it account for the direction of the applied discharge electric field. Hence, we observed that different linear polarization directions lead to different interactions between the electric field of THz pulse and DC field. Orientation of DC electric field and THz electric field can be seen Figure 5.1.

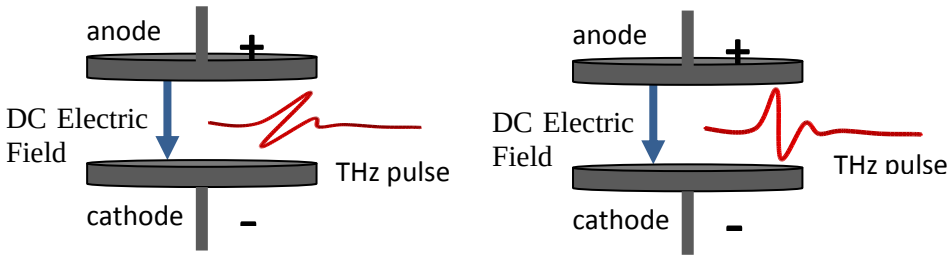

Figure 5.1: Orientation of DC electric field and THz electric field. The figure on the left hand side gives the perpendicular polarization and the figure on the right hand side gives the parallel polarization.

The polarization of the THz pulse can be changed by changing the polarization of Ti-sapphire laser pulse and rotating the dipole antenna to the intended direction. To change the polarization of the visible pulse we place a half-wave before the beam-splitter (see figure 4.2). Then we rotate both the generation and detection antenna so that their dipoles are parallel to the visible beam polarization. This condition leads to two different measurements when performing the experiments. From now on, these measurements will be named as parallel polarization if the THz field is parallel to the applied DC field and perpendicular polarization if the THz field is perpendicular to the applied DC field. In addition to changing the polarization direction of the THz beam, we also investigated what we believe to be two different regions in the DC discharge plasma: the cathode region and anode region. The reason why we can separate these regions lies in the fact that the THz beam diameter is ~5cm and the separation between the cathode and the anode plate is ~9cm so that we place one plate near the bottom of the THz beam and the other plate far away from

the top of the THz beam, roughly about 3-4 cm away. Doing this leads to the following expected distribution in the DC glow discharge plasma: If the cathode plate is at the bottom then the negative glow region and faraday dark space dominate the THz beam path, and if the anode plate is at the bottom then the positive column dominates the THz beam path. The most important region in the cathode area is the Negative Glow which is the most luminous part of the plasma; it has a high electron temperature and low electron density. Furthermore, the most important region in the anode area is the Positive Column which represents quasineutral plasma with high electron and ion density.

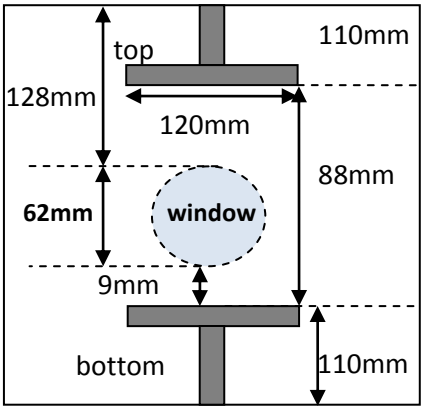

Figure 5.2: Dimensions of plasma chamber

Our experiments show that transmission of the THz pulse for all the aforementioned cases are not as we are expected from our simulations based on the Drude theory. Therefore, as our data will show, it can be concluded that plasma dielectric function cannot be explained by using simple models like the Drude Model.

As DC Glow Discharge plasmas have low electron temperatures and electron densities, they are generally known as cold plasmas. As we have shown in Chapter 3, using the Drude Model we can obtain the complex refractive index of the plasma and THz transmission through the plasma by analyzing the Fresnel coefficients for transmission and reflection. According to this model, transmission should be equal to unity since the THz frequency is much higher than the plasma frequency and collisions are not expect o play an important role in the cold plasma [60].

Initially we studied the transmission of the THz beam through an atmospheric discharge plasma. If we look at the transmission profile of the time domain THz waveform, there is a slight difference as observed between the vacuum and plasma transmission of the THz pulse as it can be seen in Figure 5.3. Because ion-electron densities of the plasma are not high enough in a DC glow discharge we don't expect the propagation through the plasma to influence the shape of the THz pulses. But as can be seen in the time domain there are differences. In this particular example the THz electric field is perpendicular to the discharge electric field. In this chapter we continue to show experiments that prove that the invalidity of using the Drude model and we qualitatively try to explain our results.

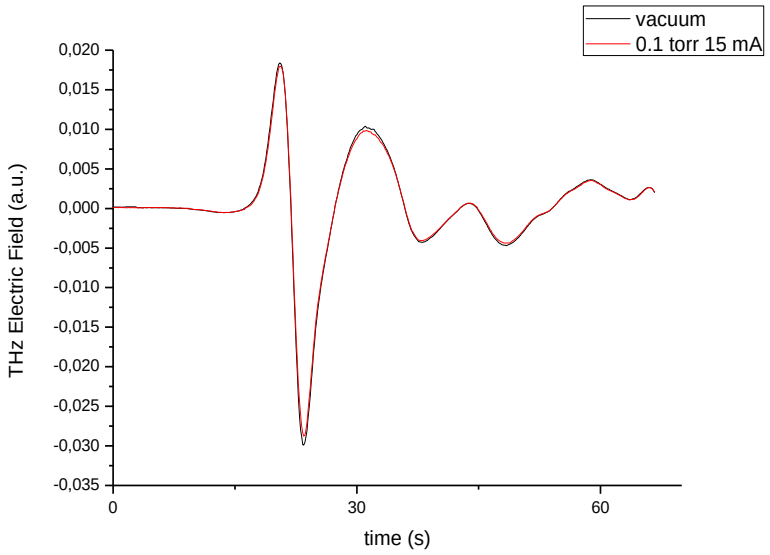

Figure 5.3: The THz pulse, passing through 0.1 torr air plasma with plasma current 15 mA and vacuum when the THz electric field is perpendicular to the DC electric field.

Not only did we perform measurements on air, but also on different gases as well. The experiments were done in the following way; first the THz transmission profile of air, N_2, and Ar plasmas were investigated for 5 mA, 10 mA and 15 mA at pressures of 0.1 Torr, 0.3 Torr and 0.5 Torr for each current (total set of 9 measurements for each gas, meaning 9 x 3 = 27 measurements). Specifically for the nitrogen and argon plasmas, due to the time it took to purge down to vacuum, our measurements at 0.5 Torr pressure were not that accurate. Thus for these

measurements we only show our values at 0.1 and 0.3 Torr. Finally, the spectral characteristics of the DC glow discharge for air, N_2, and Ar plasmas were measured between 200-1100 nm for one particular discharge current and one pressure (totaling a set of 3 measurements). These pressures were chosen accordingly to our experimental set-up so as to obtain stable plasma throughout the experiment.

Even though our THz spectrum can extend from 0.05 THz to 1.1 THz the transmission spectrum was limited between 0.05 THz to 0.4 THz since the kodiac glass we used for the windows of the plasma chamber scattered and attenuated the THz as it contains metallic particles in it.

First we performed the experiment with parallel polarization and we found that the transmission was unity for different pressures and currents. Then we performed the experiment with perpendicular polarization, and it was found that the THz transmission through Air and Nitrogen gas plasmas were considerably lower than 1 (our threshold value to say it is less than 1 was if there was more than 10% change in the transmission - at this level we are confident that the observations was not affected by noise from the environment and the laser), a result not expected due to the low electron densities and low plasma frequency. And that the transmission through the Argon gas plasma was unity, near the expected result. We also performed the above measurements for transmission through near the anode and transmission through near the cathode. These measurements were done at 0.1 and 0.3 Torr.

5.1 Air Plasma

First of all, to examine the polarization dependent interaction, we performed the experiment with parallel polarization and then we repeated it with perpendicular polarization. Afterwards we compared our results. Our experimental procedure was as follows: First the plasma chamber plates were arranged so as the THz pulse passed through close to the anode region. Then it was evacuated to 10^{-2} Torr with the rotary pump and the vacuum data was taken without the plasma. Next, air was injected from the top of the chamber and the plasma chamber pressure was set to 0.1 Torr by adjusting the valve between the pump and plasma chamber. Following this, the

plasma was generated by applying a DC bias to the electrodes and the plasma current was adjusted to 5 mA. Then, the THz was passed through the plasma and data was taken by changing the delay between the pump and probe pulse in the THz-TDS system. A photographic image of the plasma is given in Figure 5.4. Afterwards, the plasma current was changed to 10 mA by adjusting the applied bias and the data was taken again. The same procedure was done to at 15 mA, and the data was recorded. Then the applied bias was shut down and the chamber pressure was fixed to 0.3 Torr.

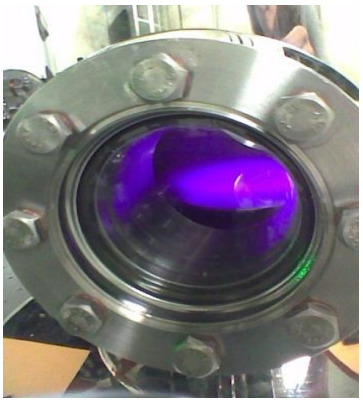

Figure 5.4: Photographic image of atmospheric plasma.

After, the plasma was generated at a plasma current of 5mA and repeated for 10 mA and 15 mA, where data was recorded for each current. In the same manner, 0.5 Torr plasma pressure data was taken at 5 mA, 10 mA and 15 mA plasma currents. Eventually, the transmission spectrum was obtained by taking the ratio of the power with and without the plasma (in vacuum). Inter electrode space in our system was set to 88 mm and the beam diameter of THz was 5 cm which allow us to investigate anode and cathode region individually.

So, after investigating the anode region with parallel polarization, we investigated the cathode region by changing the terminals of the applied DC potential. We followed the same procedure while taking cathode transmission data. The transmission spectrums of the air DC glow discharge plasma for parallel polarization through anode and cathode regions are given in Figure 5.5 and 5.6 respectively.

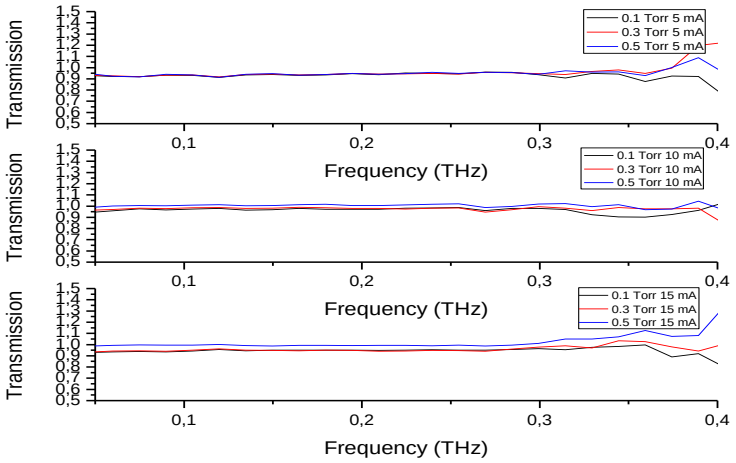

Figure 5.5: THz transmission through air DC glow discharge plasma for different pressures and plasma currents from anode region and parallel polarization.

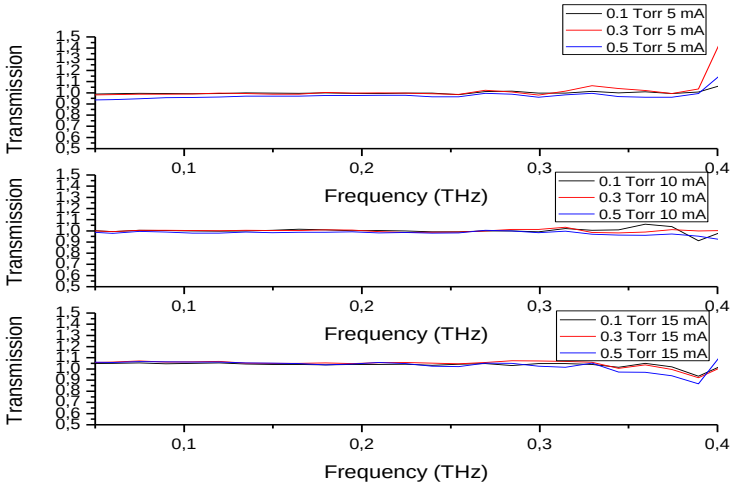

Figure 5.6: THz transmission through air DC glow discharge plasma for different pressures and plasma currents from cathode region and parallel polarization.

As can be seen from the Figure 5.5 and 5.6, the transmission spectrum was almost not affected by the plasma for differing plasma currents and pressures (at our confidence level of 10%). Also, there was not any significant difference between anode and cathode region data sets. The observed slight differences may be attributed to the power variation of laser pulse since the generated THz pulse is very sensitive to this difference. The results coincide with the Drude Model as was expected.

Afterwards, we continued by changing the parallel polarization of the THz pulse with respect to the applied DC electric field to perpendicular polarization by changing the polarization of the optical pulse from the Ti-Sapphire laser and changing the orientation of the photoconductive antenna. Then we followed the same procedure as we had done for parallel polarization. First we performed the experiments by allowing the THz pulses to pass through the anode region for the given plasma pressures and currents and then repeated the experiment for the cathode region. The transmission spectrums of the air DC glow discharge plasma for perpendicular polarization through anode and cathode regions are given in Figure 5.7 and 5.8 respectively. Transmission through the anode region is almost unity as it is clear from the Figure 5.7 which supports the Drude Model simulations we had showed previously. Therefore, it can be concluded that changing the polarization does not affect the THz transmission through the anode region (This is an initial qualitative result and further needs to be explored, due to the fact that some measurements performed by other members of our group did show a slight change in the transmission above the 10% confidence level).

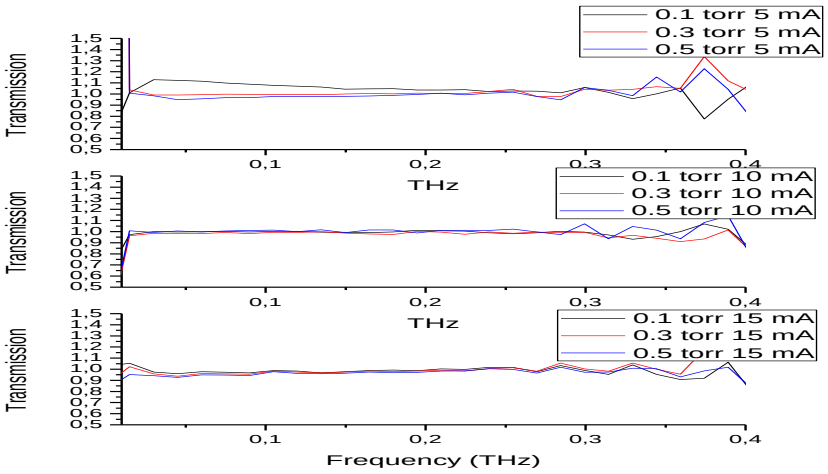

Figure 5.7: THz transmission through air DC glow discharge plasma for different pressures and plasma currents from anode region and perpendicular polarization.

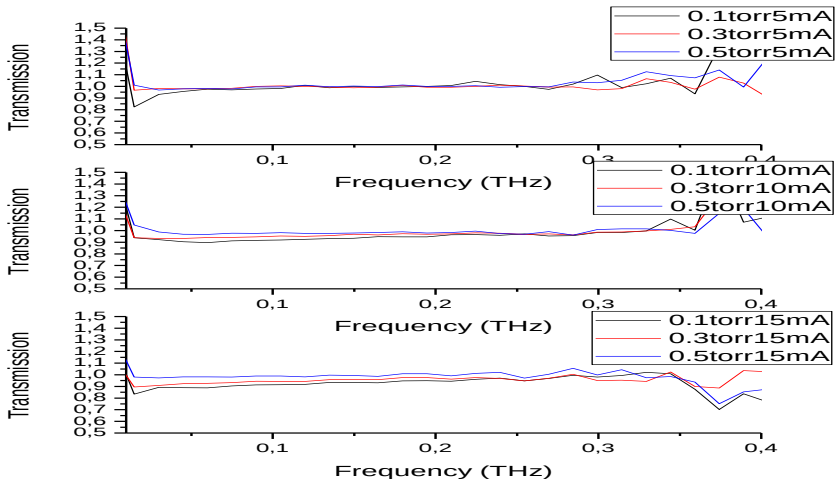

Figure 5.8: THz transmission through air DC glow discharge plasma for different pressures and plasma currents from cathode region and perpendicular polarization.

The THz transmission through the cathode region shows larger variation than that of the anode region, and especially the results obtained at 15mA discharge current (Figure 5.8) does not support the Drude Model. Transmission is significantly lower than one which is an unexpected result for us. Thus, we may conclude that there is an interaction between THz electric field and applied DC electric field for perpendicular polarization through the cathode region, however it is not a clear picture since this result is close to our confidence level of more than 10% change in transmission. As it will be shown below we see more of a drastic change for the constituent gases in the air.

We developed two qualitative theories to understand the physical mechanism behind this change in transmission. The first theory is that the oscillations of the electrons in the plasma are driven by the frequencies in the THz electric field. This driving field is more apparent when the field is perpendicular to the DC discharge field. More quantitatively this can be seen as the following: The DC discharge applied voltage in the plasma is on the order of 500V, thus one can assume there is an applied electric field strength of roughly 55 V/cm. The expected THz electric field strength is on the order of V/cm as well thus when this field is parallel to the applied DC field the DC electric field dominates, however when it is perpendicular the THz

field causes enough driving oscillations to perturb the plasma medium. Thus, electron collision frequency increases which changes the dielectric function of the plasma in turn. So the THz pulses that come after other THz pulses are affected by these changes. And since we average over many THz pulses per one data point (see chapter 4) we see the affect of this. Specifically 70 million THz pulses are incident to the plasma in a second. As our measurement time is in the order of milliseconds, some of the THz pulses oscillate the plasma and others are affected by these oscillations in the relatively long measurement time.

A second qualitative explanation is the peak power of each THz pulse in the beam. The average beam power of THz radiation is on the order of microwatts however the peak pulse power is around 1 watt. So the pulses have enough energy to oscillate the electrons in the plasma and change the collision frequency considerably. Theoretically, it has been shown that high power microwaves propagating with a polarization perpendicular to the applied plasma field can be non-linearly absorbed, that is even if the plasma frequency is lower than the microwave frequency the high power of the microwave radiation can show non-linear absorption and reduce the transmission for perpendicular polarization [61]. Both these theories suggest that there is an interaction with the applied DC plasma field and the THz electric-field. Both these affects are not included in the Drude model, when analyzing the cold plasma above the plasma frequency where the dispersion relation is real. In order to investigate these theories, we repeated this experiment for two different gases: N_2 and Ar. At the end of these experiments, as will be shown, we could only conclude that the most important factor affecting the transmission profile of THz pulses is the orientation of polarization relative to the plasma electric field.

5.2 Gas Plasma

We investigated the properties of N_2 and Ar gas DC glow discharge plasmas using two distinct methods. The first method was investigation of spectral characteristics between 200 nm- 1100 nm by using a spectrometer (Ocean Optics HR 2000) to measure the discharge spectrum with a resolution of 3 nm. The second method was based on far-IR transmission from 0.05 THz - 0.4 THz. Here the

polarization of the THz pulse was oriented perpendicular to the plasma field since this gave the largest difference in transmission as was observed in air plasma experiments. Again the transmission was limited in frequency due to the kodiac glass windows on the chamber.

5.2.1. Emission Spectrum

The emission spectrums of three different gas plasmas were studied. These were Air, N_2 and Ar plasma respectively. In each spectra, very intense emission lines are observed for each gas as it can be seen from Figure 5.9.

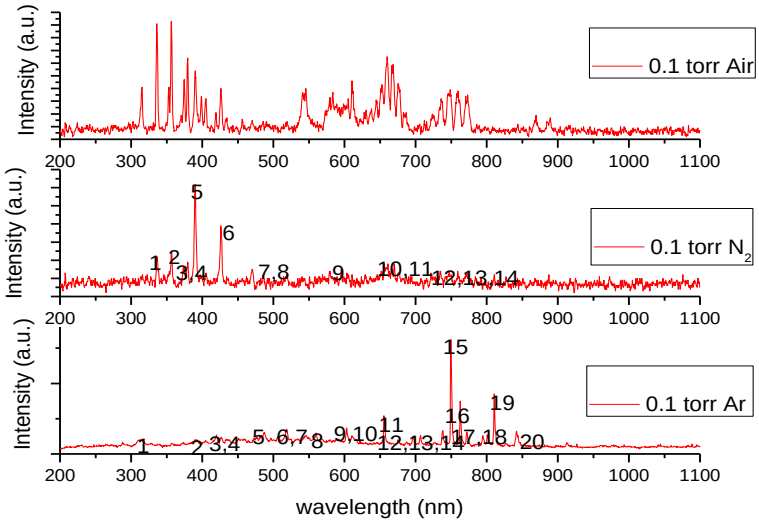

Figure 5.9: 200 nm- 1100 nm Emission Spectrum of Air, N_2 and Ar Gas Plasmas respectively

The emission spectrum for each gas was taken at a constant pressure of 0.1 Torr and a constant current 15 mA (Again these parameters were chosen according to the following: We observed the most stable plasma at 0.1 Torr, i.e. no visible fluctuations and the highest discharge current is expected to give the largest ionized species content in the gas). As can be seen from Figure 5.9, The molecular band spectra are strongly emitted, which results from the transitions among various vibrational states in different electronic states of N_2 or N_2^+ (singly ionized molecular nitrogen) [55]. The most intense line is at 391.4 nm, which is a characteristic of the

N_2 negative glow [56, 57]. Also, there are many atomic emission lines (Ar 1) and emission lines from singly ionized species (Ar 2). Atomic emission lines at 811.9 nm and 750.3 nm are observed to be dominant for argon. The numbered peaks in the emission spectrum are listed in Table 5.1 below, with their corresponding species. The number of each transition is also noted above in Figure 5.8.

Table 5.1: Observed emission lines of N_2 and Ar with their corresponding species.

	Nitrogen	
Peak Number	**Wavelength(nm)**	**Species**
1	337.1	N_2
2	357.7	N_2
3	375.5	N_2
4	380.5	N_2
5	391.4	N_2^+
6	427.7	N_2^+
7	470.9	N_2^+
8	580.4	N_2
9	595.9	N_2
10	654.4	N_2
11	670.4	N_2
12	738.6	N_2
13	762.6	N_2
14	775.3	N_2

	Argon	
Peak Number	**Wavelength (nm)**	**Species**
1	315.3	AR 2
2	390	AR 2
3	420.1	AR 1
4	426.6	AR 1
5	486.7	AR 2
6	518.7	AR 1
7	517.6	AR 2
8	560.0	AR 1
9	603.2	AR 1
10	603.0	AR 2
11	655.1	AR 2
12	696.5	AR 1
13	707.7	AR 2
14	708.6	AR 1
15	750.3	AR2
16	763.0	AR 1
17	795.7	AR1
18	800.6	AR 1
19	811.9	AR1
20	843.7	AR1

5.2.2. Transmission Spectrum

We repeated the measurements we did for the air plasma now for each gas plasma using THz-TDS. We studied the transmission of the THz beam for

perpendicular polarization only, while changing the pressure from 0.1 to 0.3 Torr at discharge currents of 5, 10, an 15mA respectively. The measurements were done for bpth transmission through the anode region and transmission through the cathode region (Again, it is important to mention that for our measurements at 0.5 Torr the plasma stability was questionable thus it may be appropriate to assume that all measurements done at 0.5 Torr, including air plasma, are questionable. However, this does not change our qualitative conclusions in the previous section).

In the figures below, while taking the transmission spectrum, the THz polarization was perpendicular to plasma electric field, plasma pressure was kept at 0.1 Torr, 0.3 Torr and the discharge current was 5 mA, 10 mA and 15 mA for eash pressure value as already stated in the beginning of this section. Because ion-electron densities of the plasma are not high enough in a DC glow discharge we don't expect the propagation through the plasma to influence transmission (as can be expected from the results of the Drude model). The transmission spectrums of nitrogen gas through anode and cathode regions are given in Figure 5.10 and Figure 5.11 respectively.

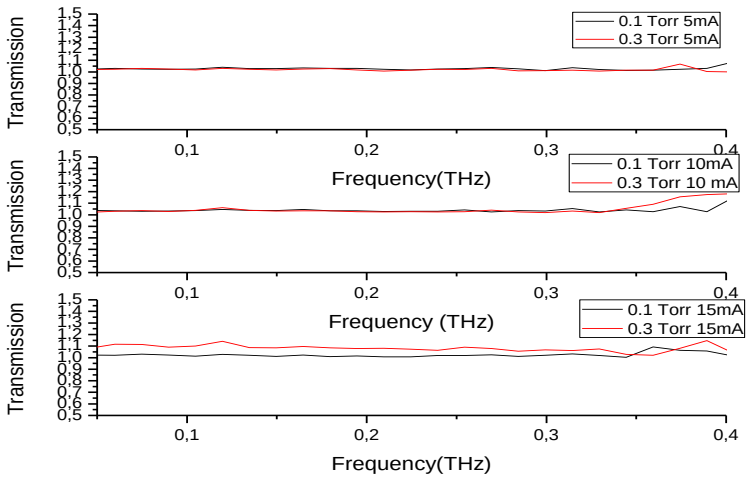

Figure 5.10: THz transmission through N_2 DC glow discharge plasma for different pressures and plasma currents from anode region and perpendicular polarization.

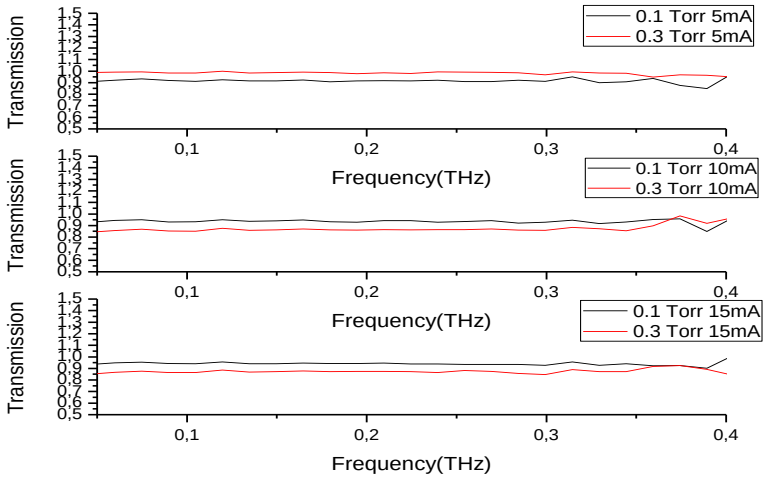

Figure 5.11: THz transmission through N_2 DC glow discharge plasma for different pressures and plasma currents from cathode region and perpendicular polarization.

As can be seen from the figures above, the transmission spectrum of N_2 though the anode region is near unity as expected. However, the transmission through the cathode region is not one for differing pressures. Thus, the transmission spectrum of N_2 discharge plasma is very similar to air plasma. This similarity can be attributed to the fact that approximately 80% of air is nitrogen. Next, the transmission spectrum of the argon discharge plasma through anode and cathode regions are given in Figure 5.12 and Figure 5.13 respectively.

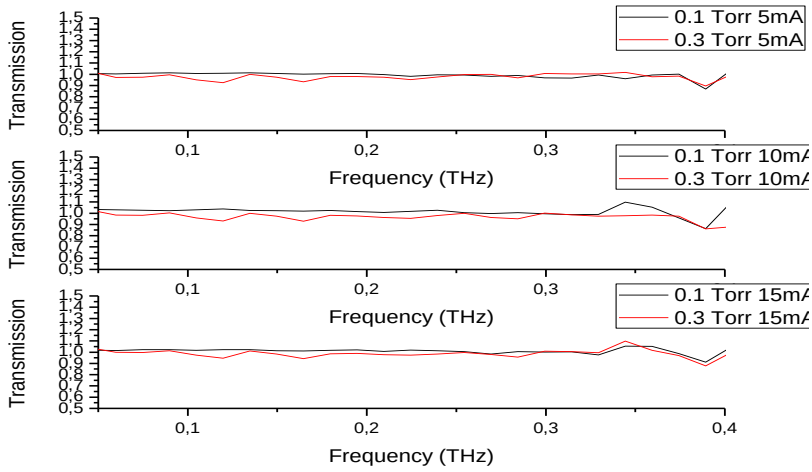

Figure 5.12: THz transmission through Ar DC glow discharge plasma for different pressures and plasma currents from anode region and perpendicular polarization.

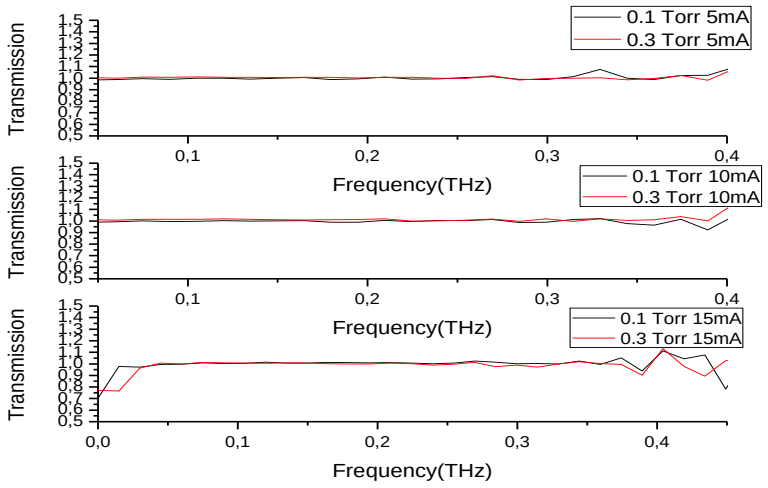

Figure 5.13: THz transmission through Ar DC glow discharge plasma for different pressures and plasma currents from cathode region and perpendicular polarization.

When we look at the transmission spectrum of the argon gas through anode and cathode regions, it is interesting to realize that both of them are near unity.

We expected to see that through anode region which includes mostly the positive column (i.e. quasineutral plasma) would support the Drude Model which tells us that the transmission should equal to unity. We saw this for all species, such as air, as well as nitrogen and argon gases. We expected the same result for the cathode region since the density, even though it is not expected to be quasineutral, is still low enough to support the Drude model dielectric function. Thus while, the transmission is near unity for the argon plasma through the cathode region, for the nitrogen and air plasma it was not. This tells us that there may be a gas-type dependent differing characteristic between argon and nitrogen (we assume air to behave similarly to nitrogen). We expect this differing characteristic to be dependent on the electric field through the gas specific cathode region plasma, since our previous results suggest that the transmission of the THz pulse is attenuated for when the THz electric field is perpendicular to the gas discharge electric field.

To understand the differences in transmission, we need to consider the internal discharge characteristics of N_2 and Ar discharge plasma in the cathode fall

region. First, ionization processes and ionization energies of them are considered. However, ionization energies for both nitrogen gas and argon are similar [58] as it can be seen from Table 5.2. Considering this, it can be concluded as there should be that there are no significant differences that exist between their electron and ion densities. Thus our measurements through the anode regions are verified: we see no observable difference between the transmission of THz perpendicular to the discharge field between argon and nitrogen discharge plasmas.

Table 5.2: Ionization processes of N_2 and Ar plasma species along with their ionization energies

Species	Ionization process	Ionization energy (eV)
N_2	$N_2 + e^- \text{ ---- } N_2^+ + 2e^-$	15,57
N_2	$N_2 + e^- \text{ ---- } N^+ + N + 2e^-$	24,50
N	$N + e^- \text{ ---- } N^+ + 2e^-$	14,50
Ar 1	$Ar + e^- \text{ ---- } Ar^+ + 2e^-$	15,76
Ar 2	$Ar^+ + e^- \text{ ---- } Ar^{+2} + 2e^-$	27,63

Next, when the cathode region is considered, there are notable differences near the cathode between argon and nitrogen. As it can be seen from Table5.3, the secondary ionization coefficient and breakdown voltage for nitrogen is high compared to argon [59]. The different transmission spectrum of the N_2 and Ar can be attributed to differences in secondary ionization coefficient and breakdown voltage. Considering the high breakdown voltage of N_2, it can be concluded that the electric field in the N_2 gas discharge plasma is higher than the electric field of Ar plasma. THz electric field which is perpendicular to plasma electric field, passing through the plasma is thought to be sensitive to this high electric field, as was qualitatively suggested from our measurements through the air plasma. According to the Rozban et.al. electric field of the incident electromagnetic wave interacts with the dc electric field of plasma that increases the electron collision rate in the plasma [67].

Table 5.3: Comparison of breakdown voltage and secondary ionization coefficient for N_2 and Ar.

	Breakdown Voltage	Secondary Ionization Coefficient
Nitrogen	high	high
Argon	low	low

Also, as we are investigating the transmission difference from the cathode region, we need to consider cathode fall potential V_c. A given cathode shows a larger V_c in molecular gases than in rare ones [48] so this statement also strengthens our argument. Also, it is of importance to note that a higher secondary ionization coefficient means a higher charge density in the cathode region, however, as was stated previously we do not expect to see such a large charge density as to affect the plasma frequency. Therefore, we can qualitatively conclude that the attenuation of the THz beam is more significant in N_2 than Ar plasma, near the cathode region since the plasma electric field near the cathode region is much higher in nitrogen than it is in argon due to nitrogen having a higher secondary ionization coefficient compared to argon. A higher electric field suggests that the THz electric field perpendicular to this field is more attenuated. This can be seen from our measurements, if you look at the cathode region perpendicular transmission for air (Figure 5.8), and nitrogen (Figure 5.11) you can see that the largest observable difference in transmission occurs at 10 and 15mA discharge current. This suggests that the higher the electric field the larger the observable change in transmission. This supports the qualitative result that the transmission is attenuated more through the cathode region of the nitrogen gas than the argon gas since the electric field there is much higher.

CHAPTER 6

CONCLUSION

We have developed an used a THz-TDS system to obtain the transmission spectrum of THz pulses through DC electrical discharge plasma. We also investigated the emission spectrum of the plasma, when the plasma was formed from various atmospheric gases. Our experimental setup allowed us to generate a plasma between 0.1- 0.5 Torr at discharge currents of 5-15 mA. Moreover, we were able to analyze the transmission of THz pulses for different orientations of their polarizations with respect to the applied DC discharge field. The THz experiments were used to characterize transmission through both the positive column and negative glow regions characteristic of a DC glow discharge. Our results suggest that the THz transmission spectra for different regions of the plasma with parallel and perpendicular polarization of THz pulses with respect to the plasma applied field do not support the Drude Model which states that for these low density plasmas the transmission should be near unity. In particular, for perpendicular polarization of the THz pulses with respect to the applied DC field, attenuation of THz radiation was observed. The discrepancy between the model and our results can be attributed to the interactions between the strength of the applied DC electric field and the THz electric field. Two mechanisms may explain the decrease in the THz field: The transmission of high power microwave radiation with polarization perpendicular to the applied plasma field has been shown to be affected, even when the microwave frequency is above the plasma frequency [61]. The second reason can be due to the THz field itself driving the plasma, by increasing the collision rate between neighboring electrons. Since there is a large ionization in regions of high applied plasma electric

field there could be more species to interact with the THz radiation, thus the scattering rate between these electrons is considerably larger than the typical values accepted for cold plasma. Thus the Drude Model is not sufficient in order to explain a DC Glow discharge which has a low electron density. The results of this thesis can be summarized as follows:

- Plasma and vacuum systems are constructed by considering the limitations of THz-TDS systems. The THz transmission spectrum and visible emission spectrum data was taken for each measurement.
- The DC Glow Discharge plasma is analyzed by the Drude Model.
- Experimentally, by considering the regions in the glow discharge, anode and cathode regions were investigated separately. Also, transmissions of parallel and perpendicular polarization of THz pulses with respect to applied plasma field were examined.
- The THz transmission shows that the THz waveform is affected by the plasma.
- Investigation of Air, N_2 and Ar plasma by passing the THz pulses through anode (positive column) and cathode (negative glow) regions was done for varying plasma pressures and discharge currents.
- THz transmission spectrum for parallel and perpendicular polarization of THz pulses (with respect to plasma applied field) for air plasma through the anode region was simply unity which agrees with the Drude Model.
- THz transmission spectrum for parallel and perpendicular polarization of THz pulses (with respect to plasma applied field) of air plasma through cathode region was lower than unity. For parallel polarization of THz pulses through cathode region, transmission is one; on the other hand transmission was lower than one for perpendicular polarization for differing pressures.
- THz transmission spectrum for perpendicular polarization of THz pulses (with respect to plasma applied field) for an N_2 plasma through anode region

was unity however it was not unity for transmission through cathode region, similar to the transmission spectrum through air plasma.

- THz transmission spectrum for perpendicular polarization (with respect to plasma applied field) of THz pulses for the Ar plasma through anode and cathode region was unity, which agrees with the Drude Model.

- Difference in transmission spectrum for perpendicular polarization (with respect to plasma applied field) of THz pulses through cathode region for N_2 and Ar plasmas could be attributed to the greater electric field in the N_2 and subsequently air plasma (since air is 78% N_2) compared to Ar plasma.

- The difference in transmission spectrum for different polarization directions of THz pulses (with respect to plasma applied field) could be understood by considering the interaction between THz pulse electric field and the applied plasma electric field. One explanation is that since the electric field of the THz pulses is perpendicular to electric field of the discharge plasma, electric field of THz pulses oscillates the electrons in the plasma which increases the collision frequency of the plasma. The effect of this phenomenon is greater when the plasma electric field is larger since there is a higher rate of ionization.

Hence, we conclude that the dynamics of the DC Glow Discharge plasma is complex and that it cannot be explained by using the Drude Model which describes the motion of electrons in a gas without considering the interaction of that gas with a probing field. In the future, the plasma dielectric function will need to be modeled taking into account these affects. In addition to these measurements, THz probes can be used to study the dynamic of RF and microwave discharge plasmas. There, the situation may be simpler since the THz field will be close to the plasma frequency, hence the Drude model may be more sufficient.

REFERENCES

1. Matthew C. Beard, Gordon M. Turner, and Charles A. Schmuttenmaer, J. Phys. Chem. B, 106, pp.7146-7159 (2002).

2. J. C. Wiltse, IEEE Transactions on Microwave Theory and Techniques, Vol. 32, N.9, pp.1118-1127 (1984).

3. M.F. Kimmit, Journal of Biological Physics, 29, pp.77–85 (2003).

4. P.P. Vasil'ev, Sov. J. Quantum Electron, Vol.20 (3) (1990).

5. Terahertz Optoelectronics, in: Topics in Applied Physics, Vol. 97, ed. by Kiyomi Sakai (Berlin, Springer-Verlag, 2005).

6. M. Tani, Y. Hirota, C. T. Que, S. Tanaka, R. Hattori, M. Yamaguchi, S. Nishizawa and M. Hangyo, International Journal of Infrared and Millimeter Waves, Vol.27, N.4, pp.531-546 (2006).

7. P. R. Smith, D. H. Auston, and M. Nuss, IEEE Journal of Quantum Electronics, Vol.24, N.2 (1988).

8. Terahertz Spectroscopy, in: Optical Science and Engineering, Vol.131 ed. by Susan L. Dexheimer (Newyork, CRC Press, 2008).

9. D. Dragoman, M. Dragoman, Progress in Quantum Electronics, 28, pp.1–66 (2004).

10. Q. Wu and X.-C. Zhang, Appl. Phys. Lett., Vol.67, N.24 (1995).

11. D. H. Auston and K. P. Cheung, J. Opt. Soc. Am. B, Vol.2, N.4 (1985).

12. Q. Wu and X.-C. Zhang, Appl. Phys. Lett., Vol.67, N.24, pp.3523-3525 (1995).

13. P.H. Siegel, IEEE Transactions on Microwave Theory and Techniques, 50, pp.910-928 (2002).

14. D. Mittleman, Nature, Vol.444, N.30 (2006).

15. C. A. Schmuttenmaer, Chem. Rev., Vol.104, pp.1759-1779 (2004).

16. B. Ferguson and X.-C.Zhang, Nature Materials, Vol.1, pp. 26-33 (2002).

17. M. Tani, M. Herrmann and K. Sakai, Meas. Sci. Technol., Vol.13, pp. 1739–1745 (2002).

18. M. Tonouchi, Nature Photonics, Vol.1 (2007).

19. B. H. Kolner, Mater. Res. Soc. Symp. Proc., Vol.1163 (2009).

20. B. H. Kolner, P. M. Conklin, R. A. Buckles, N. K. Fontaine, and R. P. Scott, Applied Physics Lett., Vol.87, 151501 (2005)

21. G. Zhao, R. N. Schouten, N. van der Valk, W. Th. Wenckebach, and P. C. M. Planken, Review of Scientific Instruments, Vol.73, N.4 (2002).

22. Daniel M. Mittleman and R. Alan Cheville

23. M. Tani, S. Matsuura, K. Sakai, and S. Nakashima, Applied Optics, Vol.36, N.30 (1997).

24. L. Duvillaret, F. Garet, J. F. Roux and J. L. Coutaz, IEEE J. Sel. Top. Quantum Electron, Vol.7, pp.615–623 (2001).

25. H. Harde and D. Grischkowsky, Journal of Optics Society of Amerika,Vol. 8, pp.1642–1651 (1991).

26. D. Grischkowsky, S. Keiding, M. van Exter, and C. Fattinger, Journal of Optics Society of Amerika B, Vol.7, N.10 (1990).

27. M. C. Beard, G. M. Turner, and C. A. Schmuttenmaer, Journal of Applied Physics, Vol.90, N.12 (2001).

28. M. Hoffmann, dissertation "Novel Techniques in THz-Time-Domain-Spectroscopy - A comprehensive study of technical improvements to THz-TDS, submitted to FakultÄat fÄur Mathematik und Physik der Albert-Ludwigs-UniversitÄat Freiburg im Breisgau.

29. Yale University, http://www.chem.yale.edu/~cas/ZnTe.html, last visited on May 2010.

30. S. Kono, M. Tani, and K. Sakai, Applied Physics Letters, Vol.79, N.7, (2001).

31. C. Kubler, R. Huber and A. Leitenstorfer, Semicond. Sci. Technol., Vol.20, pp.128–133 (2005).

32. K. Wynne, Ultrafast Terahertz Pulses: A Booming Technology

33. Z. Wang, IEEE Transactions on Geoscience and Remote Sensing, Vol.1, N.1 (2002).

34. A. Nahata, A. S. Weling, and T. F. Heinz, Appl. Phys. Lett., Vol.69, N.16 (1996).

35. H. J. Bakker, G. C. Cho, H. Kurz, Q. Wu and X.-C. Zhang, J. Opt. Soc. Am. B, Vol.15, N.6 (1998).

36. P. Uhd Jepsen, R. H. Jacobsen, and S. R. Keiding, J. Opt. Soc. Am. B, Vol.13, N.11 (1996).

37. S. Kono, M. Tani, P. Gu, and K. Sakai, Applied Physics Letters, Vol.77, N.25 (2000).

38. M. Tani, K.-S. Lee, and X.-C. Zhang, Applied Physics Letters, Vol.77, N.9 (2000).

39. Q. Wu and X.-C. Zhang, Appl. Phys. Lett., Vol.68, N.12 (1996).

40. Q. Wu and X.-C. Zhang, Appl. Phys. Lett., Vol.70 (1997).

41. S.-G. Park, M. R. Melloch, and A. M. Weiner, IEEE Journal of Quantum Electronics, Vol.35, N.5 (1999).

42. Y. Cai, I. Brener, J. Lopata, J. Wynn, L. Pfeiffer, J. B. Stark, Q. Wu, X. C. Zhang, and J. F. Federici, Applied Physics Letters, Vol.73, N.4 (1998).

43. S.-G. Park, M. R. Melloch, and A. M. Weiner, Applied Physics Letters, Vol.73, N.22 (1998).

44. Plasma Physics and Controlled Fusion, 2nd edition, F. Chen (New York, Plenum Press 1984).

45. The Glow Discharge, 1st edition, B. L. Worsnop (London, Methuen and CO LTD 1966

46. A. Bogaerts and R. Gijbels, Spectrochimica Acta Part B, Vol.53, pp.1-42 (1998).

47. A. A. Garamoon, A. Samir, F. F. Elakshar and E. F. Kotp, Plasma Sources Sci. Technol., Vol.12, pp.417–420 (2003).

48. Ionized Gases, 2nd Edition, A. von Engel (Oxford, Oxford-Clarendon Press, 1965).

49. A. Qayyum, S. Zeb, S. Ali, A. Waheed, and M. Zakaullah, Plasma Chemistry and Plasma Processing, Vol.25, N.5 (2005).

50. J. L. Zhang, X. L. Deng, P. S. Wang and T. C. Ma, Vacuum, Vol.59, pp.80-87 (2000).

51. P. G. Reyes, E. Mendez and F. Castillo, Study of the Plasma Emission Lines of Different Pressure of Gas

52. J. D. Jackson, Classical Electrodynamics, 3rd Edition, 1998, Wiley press.

53. Stanford Research Systems, http://www.thinksrs.com/downloads/PDFs/Manuals/SR530m.pdf, last visited on May 2010.

54. B. H. Kolner,P. M. Conklin, R. A. Buckles, N. K. Fontaine, and R. P. Scott, Applied Physics Letters, Vol.15, N.87, (2005).

55. K. Wagatsuma and K. Hirokawa, Anal. Chem., N.57, pp.2901-2907 (1985).

56. S. P. Brühl, M. W. Russell, B. J. Gomez, G. M. Grigioni, J. N. Feugeas, and A. Ricard, J. Phys. D: Appl. Phys, Vol.30, pp.2917-2922 (1997).

57. L. Petitjeani and A. Ricard, J. Phys. D: Appl. Phys., N.17, pp.919-929 (1984).

58. A. A. Garamoon, A. Samir, F. F. Elakshar and E. F. Kotp, Plasma Sources Science and Technology, Vol.12, pp.417-420 (2003).

59. G. Petraconi, H. S. Maciel, R. S. Pessoa, G. Murakami, M. Massi, C. Otani, W. M. I. Uruchi, and B.N. Sismanoglu, Brazilian Journal of Physics, Vol.34 (2004).

60. S. P. Jamison, J. Shen, D. R. Jones, R. C. Issac, B. Ersfeld, D. Clark, and D. A. Jaroszynski, Journal of Applied Physics, Vol.93, N.7 (2003).

61. B. S. Lazebnik, G. A. Markov, and I. V. Khazanov, Scientific-Research Institute of Radiophysics, Radiofizika, Vol.19, N.8, pp.1246-1251, (1976).

62. Batop Optpelectronics, http://www.batop.de/products/photoconductive-antenna/data-sheet/manual_PCA-44-06-10-800.pdf, last visited on May 2010.

63. Batop Optpelectronics, http://www.batop.de/products/photoconductive-antenna/data-sheet/manual_PCA-40-05-10-800.pdf, last visited on May 2010.

64. A. Dinklage, T.Klinger, G. Marx, L. Schweikhard, Plasma Physics: Confinement, Transport and Collective Effects, Springer Berlin, 2005

65. Wikipedia, http://en.wikipedia.org/wiki/File:Paschen_Curves.PNG, last visited on May 2010.

66. University at Buffalo, http://www.acsu.buffalo.edu/~solabisi/Shola/, last visited on July 2009.

67. D. Rozban, N. S. Kopeika, A. Abramovich, and E. Farber, Journal of Applied Physics, Vol. 103, N.093306, 2008.